Astron. Astrophys. 326, 347–365 (1997)

ASTRONOMY
AND
ASTROPHYSICS

A molecular line and infrared study of NGC 2264 IRS 1

K. Schreyer[1], **F.P. Helmich**[2], **E.F. van Dishoeck**[2], **and Th. Henning**[1]

[1] Max Planck Society, Research Unit "Dust in Star-forming Regions", Schillergäßchen 2-3, D-07745 Jena, Germany
[2] Leiden Observatory, P.O. Box 9513, 2300 RA Leiden, The Netherlands

Received 22 November 1996 / Accepted 24 April 1997

Abstract. We present a study of the region around the intermediate-mass young stellar object NGC 2264 IRS1. This source is embedded in a dense cloud core. Infrared images in the J, H, and K band show a jet-like structure connected with IRS1 as well as a second very deeply embedded small star cluster to the southeastern side. IRS1 itself is surrounded by a number of embedded low-mass stars. We mapped this area in various CS transitions, CO 3→2, some methanol lines and in $C^{18}O$ 2→1. The mapping results clearly show a second cloud clump centered at the small star cluster. Two molecular outflows were found in the observed region. One flow is oriented along our line of sight and associated with IRS1 and the other flow is centered at the small star cluster.

Several additional spectral line settings were taken at the IRS1 position to get more accurate constraints on the gas temperature and density. These data, as well as the maps, were analysed with statistical equilibrium excitation calculations. The best fit results give an uniform temperature of about 55 K in a quite large inner cloud region ($1' \times 1'$), with even warmer gas (>70 K) present close to IRS1 and the embedded star cluster. This warm cloud core is surrounded by extended material at a temperature of 20 to 30 K. Radiative transfer models applied for different molecules constrain the mean central density to 2 10^6 cm^{-3}.

We estimated the beam-averaged total H_2 column densities at a number of grid positions around IRS1 from the $C^{18}O$ measurements. Using the modeled CS excitation, we can constrain the beam-averaged CS abundance distribution over the same area. The inferred CS abundance with respect to H_2 of 1 10^{-9} is nearly constant over the whole region, and there is no indication for a CS depletion on this scale.

Observations of a large number of other molecules have been obtained as well at the IRS1 position. The resulting abundances are compared to those found in other high- and low-mass young stellar objects. The abundances of the organic molecules H_2CO and CH_3OH are somewhat enhanced, whereas those of sulfur-bearing molecules are much lower. The most striking characteristic of the NGC 2264 chemistry is its nitrogen chemistry, especially the very high abundances of N_2H^+ and N_2. These results suggest that NGC 2264 is in a somewhat later evolutionary stage.

Key words: ISM: clouds – ISM: NGC 2264 cloud – stars: formation – radio lines: ISM – infrared: ISM: continuum – ISM: molecules

Send offprint requests to: K. Schreyer

1. Introduction

It is well established that dense cores in molecular clouds are the sites of recent star formation. In order to probe the physical and chemical conditions in the very dense gas surrounding protostars and young stellar objects (YSOs), high-resolution (sub-)millimeter-wave observations of molecules with large dipole moments (and thus high critical densities) are necessary. The line shapes also provide direct kinematic information of the gas motion in the immediate environment of the YSOs (Zhou et al. 1993; van Langevelde et al. 1994). A particularly useful molecule in this respect is CS, since the higher CS 5→4 and 7→6 transitions trace the densest regions up to 10^7 cm^{-3} and the lower 3→2 and 2→1 lines the less dense gas with 10^4-10^5 cm^{-3}, thus covering a large range in densities. In order to test theories of the physical and chemical structure of YSOs, it is important to study relatively isolated objects which are not influenced by the formation of other stars in the close neighborhood.

The near-infrared source NGC 2264 IRS1 is a relatively isolated luminous infrared source (distance 800pc) in the star-forming region NGC 2264 (Fig. 1) which belongs to the larger infrared Mon OB1 Stellar Loop (Schwartz 1987). Different observations (Schwartz et al. 1985, Krügel et al. 1987, Phillips et al. 1988) suggest that IRS1 (Allen 1972) is a very young star which is located in a molecular core of high density embedded in a more extended CO envelope. Greene et al. (1990) reported 2.2 μm observations of IRS1. They found only one IR source in an area of $1'$ around IRS1. Harvey et al. (1977) estimated a 2-200 μm luminosity of $\approx$ 3500 $L_\odot$. This luminosity is in between high-mass young stellar objects such as IRc2 in Orion

and low-mass objects such as L1551 IRS5 in Taurus. The luminosity of IRS1 implies an early B-type star (Schwartz et al. 1985).

Schwartz et al. (1985) reported CO, CS, and NH_3 observations of NGC 2264 suggesting that IRS1 is located in a clump which has formed within a rotating ring-shaped molecular cloud. This source heats the immediate environment and ionizes a small H II region. The CO $J = 7 \rightarrow 6$ measurements by Krügel et al. (1989) imply high-density and temperature gas at the IRS1 position to excite the $J = 7$ level. The combination of the 1.3 mm observations by Chini et al. (1986) and the 3.3 mm measurements by Schwartz (1980) may indicate the presence of a steep temperature gradient in the outer layers of the dust core. The free-free emission is negligible at these wavelenghts (Walker et al. 1990).

Bally & Lada (1983) found a high-velocity CO outflow produced by IRS1. In contrast to Schwartz et al. (1985) and Bally & Lada (1983), Krügel et al. (1987) do not find any evidence for a large-scale gas rotation, nor any clear association of red and blue wing emission with IRS1. They reported that the cloud in which IRS1 is embedded consists of at least three subclouds with different velocities. Phillips & Mampaso (1991) again searched for a CO outflow in this region and noted that the blue flow is much more constrained by ambient material than the red flow. They also discussed that there appear to be at least three other discrete regions of blue line emission.

Additional evidence for star-forming activity near IRS1 comes from observations of maser emission. Haschick et al. (1990) found strong methanol maser emission at the position RA(1950) = $06^h\ 38^m\ 24.9^s$ and Dec(1950) = $09^\circ\ 32'\ 28''$ close to IRS1, whereas Henning et al. (1992) reported the presence of an H_2O maser at the position of the IRAS source 06384+0932 (RA(1950) = $06^h\ 38^m\ 26.2^s$ and Dec(1950) = $09^\circ\ 32'\ 25''$), slightly offset from IRS1.

In this paper, we present molecular line observations around the central cloud core of NGC 2264 IRS1. We mapped the inner cloud part in CS $7 \rightarrow 6$, $5 \rightarrow 4$, $3 \rightarrow 2$, $2 \rightarrow 1$, $C^{18}O$ $2 \rightarrow 1$, and in some transitions of CH_3OH to get information about the density distribution and the velocity field. Additionally, we observed H_2CO at different positions, which is very useful to constrain density and temperature. Previous observations have much lower spatial resolution and/or probe much less dense material than those presented in this paper.

One aim of this work is to compare the physical conditions in this cloud, which has formed a somewhat less luminous star, with cores which have formed more massive stars like W 3 (Wink et al. 1994; Helmich et al. 1994), AFGL 2591 (Carr et al. 1995) and NGC 2024 (Mauersberger et al. 1992), as well as cores of low-mass star formation like IRAS 16293-2422 (Mundy et al. 1992, Blake et al. 1994, van Dishoeck et al. 1995) and NGC 1333/IRAS 4 (Blake et al. 1995). A second aim is to search for changes in the abundance of CS in the more inner cloud part. CS is often used as a tracer of dense gas, where its abundance is assumed to be relatively constant (Walker et al. 1994). Evidence for a decreased CS abundance in the high-density disk-like structure around HL Tauri was reported by Blake et al. (1992) in interferometer observations. It indicates a strong interaction between the molecules and the grain surfaces through depletion of gas phase molecules onto grain mantles at high densities and possible transformation of molecules by chemical reactions.

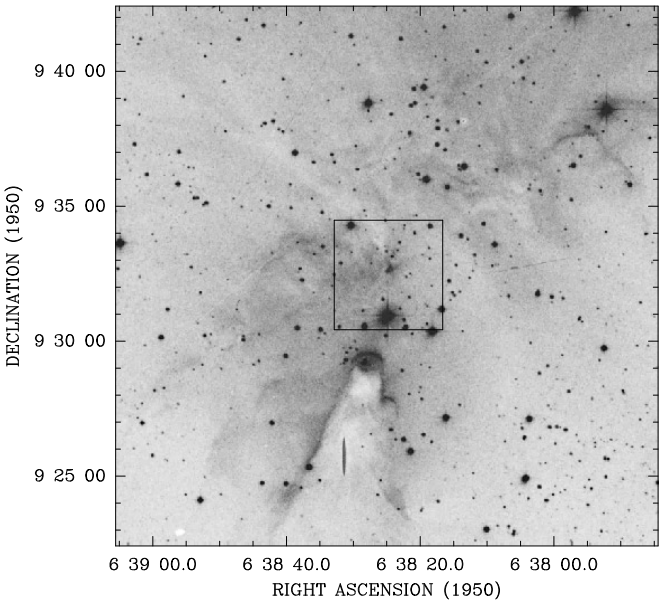

Fig. 1. "Optical picture" of the region NGC 2264 IRS1 taken from the Palomar Sky Survey (The Digitized Sky Survey). The black box in the centre of the figure indicates the sky area of the infrared images in Fig. 2.

A further aim is to get a more detailed chemical overview of this star-forming core, since it has been found that the chemical composition depends sensitively on the evolutionary state of the object (van Dishoeck et al. 1993). Thus, we searched for various other molecules at the IRS1 position to determine the molecular abundances of the dense gas. The results will be compared with other recent chemical studies such as that of the high-mass W 3 region by Helmich & van Dishoeck (1997), the intermediate-mass regions IRAS 05338-0624 and Serpens by McMullin et al. (1994a,b), and the low-mass object IRAS 16293-2422 (Blake et al. 1994, van Dishoeck et al. 1995). The ion and electron fraction in the NGC 2264 core have already been studied extensively by de Boisanger et al. (1996).

2. Observations

2.1. Infrared imaging

We performed infrared imaging at J, H, and K using the MAGIC(Black)-camera (Herbst et al. 1993, Herbst & Rayner 1994) on the 2.2-m telescope at Calar Alto, Spain, in January 1995. The detector was a NICMOS3-Array of 256×256 pixels which covers a field of view of 163.8 square arcseconds. Thus, the image resolution corresponds to $0.64''$ per pixel. To produce the infrared images, we used three filters: J (1.13-1.37 μm), H (1.50-1.80 μm), and K (2.00-2.40 μm). The H and K images

were built by 4 single frames, the J image by 2 single frames, which were merged to one resulting mosaic image. Every single frame is an average of single snapshots with integration times of 10 seconds for J, 0.2 seconds for H, and 0.1 seconds for K. We produced 6 snapshots for the J images and 127 snapshots for H and K. The different integration times are caused by the saturation properties of the array pixels. We chose the shortest integration time in the K band because IRS1 is brighter in K than in H and J. The total integration time for IRS1 resulted in 3 minutes in J, 2.41 minutes in H, and 50.8 seconds in K.

2.2. Line observations

We mapped the region around NGC 2264 IRS1 in CS 5→4, CS 7→6, $C^{18}O$ 2→1, CO 3→2 and several components of methanol $5_K \rightarrow 4_K$ with the James Clerk Maxwell Telescope (JCMT)[1] at Mauna Kea, Hawaii, in February 1994. Additionally, we measured some spectral line settings on the position of IRS1. These are summarized in Table 1.

We used the facility receivers A2(216-280 GHz), B3i (300-380 GHz), and C2 (450-500 GHz) as the frontends with the Digital Autocorrelation Spectrometer (DAS) as the backend. For the mapping, the total bandwidth was 500 MHz for $C^{18}O$ 2→1 and 250 MHz for the CS transitions, centered at V_{LSR} = +8.3 km s^{-1}. The corresponding velocity resolution is 0.14 km s^{-1} for $C^{18}O$ and 0.2 km s^{-1} for the CS transitions. The CS 7→6 line at 342.883 GHz was placed in the lower sideband so that the ^{12}CO 3→2 line at 345.330 GHz could be observed simultaneously in the upper sideband. Similarly, the CS 5→4 setting at 244.936 GHz in the upper sideband also covered several components of the $5_K \rightarrow 4_K$ band of CH_3OH at 241.9 GHz in the lower sideband. Furthermore, the CS 10→9 line at 489.751 GHz was searched together with the $C^{34}S$ 10→9 line at 481.916 GHz in the opposite sideband.

The telescope half power beamwidth covered 12″ for the 492 GHz window, 15″ for 345 GHz, and 21″ for the 220 GHz band. In February 1994, the main beam efficiencies η_{mb} were 0.35 at 492 GHz, 0.45 at 345 GHz, and 0.53 at 220 GHz as measured from planets and standard sources. In subsequent runs, the efficiencies were increased to 0.58 and 0.70 for receivers B3i and A2 respectively. The line intensities were calibrated by the chopper-wheel method (Kutner & Ulich 1981) to produce line strengths on the antenna temperature (T_A^*) scale. The main beam temperature is $T_{mb} = T_A^*/\eta_{mb}$. The pointing was checked every two to three hours with the source OMC 1, and was found to be accurate to better than 5″.

The observations for the CO and CS maps were made in the position-switch mode with an off-position of 10′ to the east for the CS transitions and an off-position of 20′ for $C^{18}O$ 2→1. The former switch is sufficient for the higher-excitation lines of the rarer molecules. The maps were sampled at half beamwidth intervals of 7.5″ for the CS 7→6 transition, and at 15″ spacing for the 220 GHz transitions. For all three mapped transitions, we used an on+off total integration time of 4 min, resulting in an rms of 0.08 K per channel at 220-240 GHz, and 0.3 K per channel at 330-345 GHz. The observations of the other molecules were either done by position-switching 10′ to the east, or by beam-switching 3′ in azimuth.

In order to get more information about the excitation of the lower CS transitions, we performed observations with the IRAM[2] 30-m telescope on the Pico Veleta, Spain, in May and October 1995. Additionally, we obtained some line settings of H_2CO, SiO, and CH_3CN (Table 1). The region of 2′×2′ around IRS1 has been mapped simultaneously in CS 2→1, CS 3→2, and $C^{18}O$ 2→1 with a spacing of 15″ in the outer regions and 7.5″ in the centre of the map. The beamsizes were 25″ at 95.017 GHz, 17″ at 142.523 GHz, and 11″ at 219.560 GHz. The backend consisted of an autocorrelator split into 3 subbands with a resolution of 40 kHz for the CS lines and 80 kHz for $C^{18}O$. The chopper-wheel method was applied to calibrate the spectra in values of T_A^*. We changed the intensities of the spectra to main beam temperatures $T_{mb} = T_A^*/\eta_{mb}$. For the values of η_{mb}, we refer to the *IRAM Newsletter, Nr. 18, 1994*. The adopted main beam efficiencies were 0.72, 0.55, and 0.41, respectively. The spectra were taken as on/off measurements with an off-position of 30 arcmin to the east and with a total integation time of 2.25 min. Pointing checks have been done about every 1.5 h depending on weather conditions and the elevation of the telescope. Typically, the pointing accuracy was somewhat better than 3″ in May 1995. In October 1995, the weather conditions were too bad to get an acceptable pointing. However, the pointing error should be less than 10″. Therefore, we only integrated at the positions of IRS1 and the small star cluster in that run.

3. Images

3.1. Infrared images

Fig. 2 shows the infrared mosaic images in J, H, and K after the sky background subtraction. The H- and K-band images cover an area of 4 square arcminutes, whereas the mosaic image in the J band does not fill this region completely. The black box in Fig. 1 helps in finding the imaged region. The source IRS1 is located in the centre of the Figs. 2a-c and the bright (optical) star W 178 is close to the lower margin. It is interesting to note that IRS1 shows a jet-like structure to the north-west in all three infrared bands. In the J band, the jet is very weak and only just above the noise. The first evidence for such a jet-like structure was recently found by Hodapp (1994). The feature looks twisted (Fig. 2.), especially in the zoomed figure. Another interesting feature which is important for our analysis is a small star cluster southeast of IRS1. This cluster must be very deeply embedded, because it can be clearly seen in the K-band image only.

In order to get more information about the degree of embeddedness of the stars in the region around IRS1 as well as their infrared excess, we produced a colour-colour diagram shown

[1] JCMT is operated by the Joint Astronomy Center on behalf of the Particle Physics and Astronomy Research Council of the United Kingdom, the Netherlands Organization for Scientific Research, and the National Research Council of Canada.

[2] Institut de Radio Astronomie Millimétrique

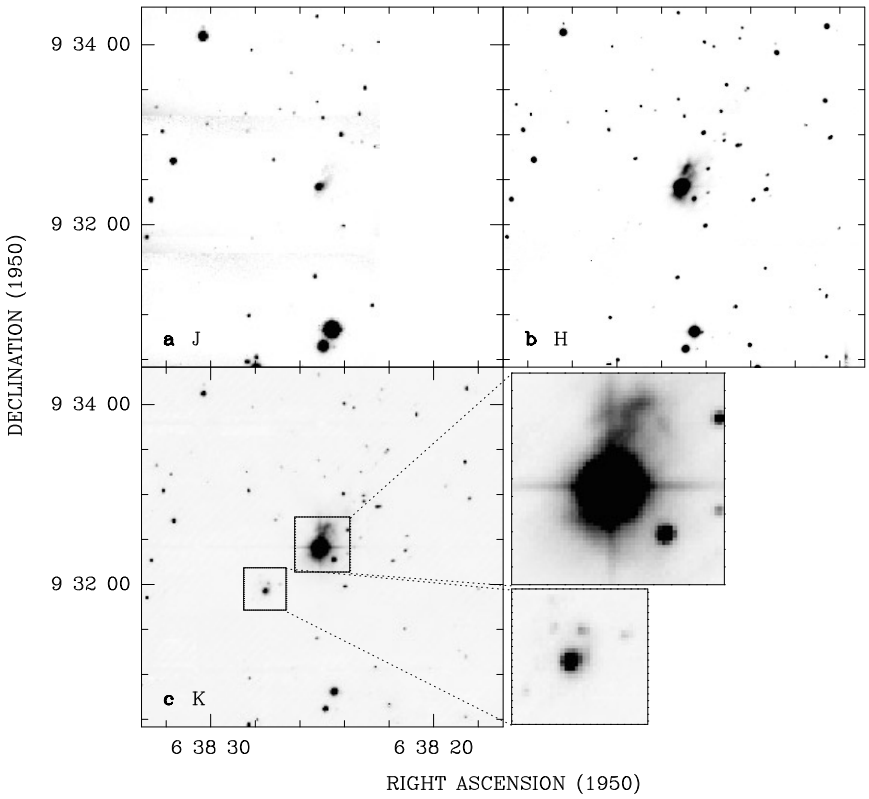

Fig. 2. a J (1.2 μm), **b** H (1.65 μm), and **c** K (2.2 μm) band mosaic images of NGC 2264. IRS1 is located in the centre of the pictures at the position of RA(1950) = $06^h\ 38^m\ 24.9^s$ and Dec(1950) = $09^\circ\ 32'\ 29''$ (Allen 1972, Allen et al. 1977). The zoomed figures show the IRS1 source and the small star cluster.

in Fig. 3. For the source exctraction and the aperture photometry, we used the Munich Image Data Analysis System and the routine DAOPHOT. The photometry was performed on each individual frame and the magnitudes were determined for each star. In the overlapping image regions, the magnitudes were compared and statistical photometric errors of $\leq$0.2 mag for J, $\leq$0.15 mag for H, and $\leq$0.08 mag for K were found. The photometric calibration was established by observations of the bright standard stars HD 40335 and HD44612. The general photometric scale for the NGC 2264 observations was fixed by adopting the J, H, and K magnitudes for both standards given by Elias et al. (1982). For IRS1 itself it was not possible to estimate the magniudes because this object was saturated.

In Fig. 3, we show (J-K) vs. (H-K) for all stars for which we obtained magnitudes in all three bands. Due to the fact that many stars found in K were not detected in J, the more deeply embedded stars are missing in the colour-colour diagram. Especially for the small star cluster, we could extract only one member for which magnitudes in all three filters are avaible. Photometry at longer wavelengths would give more constraints on these stars which are very good candidates for objects being in an early evolutionary stage.

In addition, the positions of unreddened main-sequence stars (Bressel & Brett 1988) are plotted in Fig. 3 as well as the reddening vectors for a B8 and a M0 star. Here, we assume the standard ratio of $E(J\text{-}H)/E(H\text{-}K)$ = 1.6 (Mathis 1990). The crosses (+) indicate the reddening shifts of these two types of main-sequence stars corresponding to a value of 5, 10, 15, 20, 25, and 30 magnitudes of visual extinction following the ratios between A_V and $E(H\text{-}K)$ given by Bressel & Brett (1988).

If we compare our colour-colour diagram with the results of the extended J, H, and K survey of NGC 2264 by Lada et al. (1993) and with the results of the (unreddened) standard disk models by Lada & Adams (1992), we find that most of the infrared sources in the immediate environment of IRS1 (marked with $\times$ in Fig. 3) show near-infrared colours similar of those of T Tauri and Herbig Ae Be stars. Therefore, we conclude that the stars in our diagram which lie to the right of the reddening band of normal stellar photospheres are young stellar objects surrounded by circumstellar matter.

For the "other" stars which are further away from IRS1 (in the projection), the situation is not so clear. Lada et al. (1993) already discussed that one cannot really distinguish between stars with circumstellar disks and spectral types between K0 and M5 and reddened stars of spectral types between A0 and K0 but without disks because both groups occupy the same area of the colour-colour diagram. Since we cannot exclude that some of the stars in our sample are reddened field stars, we assume that our group of "other" stars contains members of both groups. Furthermore, a number of these "other" stars which are located to the right of the reddening band seem to be well fitted by the simple disk models presented and discussed by Lada et al. (1993) and Lada & Adams (1992) (for a more detailed discussion of disk radiation see Menshchikov & Henning 1996).

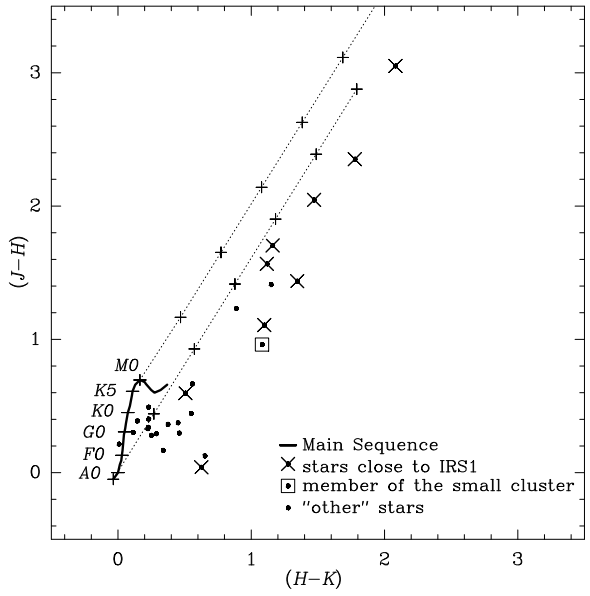

Fig. 3. The HJK colour-colour diagram for the region around NGC 2264 IRS1. The solid curve in the lower-left figure part is the unreddened main sequence (Bessel & Brett, 1988). The two dashed lines show the reddening vector where the plotted crosses (+) indicate the shifts of the main-sequence stars corresponding to 5, 10, 15, 20, 25, and 30 magnitudes of visual extinction. Stars which are located in the immediate environment of IRS1 are overplotted with crosses (×). The only member of the small star cluster for which the H, J, and K magnitudes are avaible is indicated by ⊡. All other stars are plotted with dots (•).

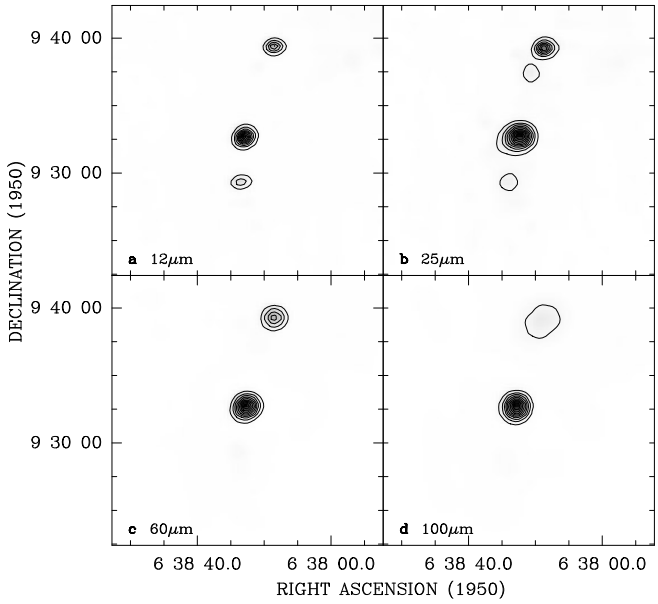

Fig. 4a–d. HIRAS images with the maximum entropy imaging algorithm (HIRAS) using the Groningen IRAS Software Telescope for all four IRAS bands. IRS1 is located in the centre of the pictures. Levels are 10 to 90% of the intensity maximum: **a** 12μm band: peak value = 203.5 MJy sr^{-1}, **b** 25μm band: peak value = 270.3 MJy sr^{-1}, **c** 60μm band: peak value = 3445.2 MJy sr^{-1}, **d** 100μm band: peak value = 7545.9 MJy sr^{-1}.

3.2. HIRAS images

We produced high-resolution infrared images with a maximum entropy imaging algorithm (HIRAS) using the Groningen IRAS Software Telescope (Assendorp et al. 1995)[3] for all four IRAS bands to get an overview of the large-scale structure of NGC 2264. Fig. 4 presents the results. IRS1 is located in the centre of the pictures. The HIRAS procedure does not resolve any structure towards IRS1 and the small star cluster. We could only find a single flux maximum near the IRS1 position which is associated with the IRAS source 06384+0932. The upper infrared source is NGC 2264 IRS2 (IRAS source 06382+0939) located in the northern cloud clump (Schwartz et al. 1985, Castelaz & Grasdalen 1988, Mendoza et al. 1990). The infrared "source" to the south of IRS1 is the Cone Nebula's head (see Fig. 1). Fig. 1 and 4 cover the same sky area. In the area of the near-infrared images (Fig. 2-3), IRS1 is the only infrared point source which was detected by the IRAS satellite. Higher spatial resolution observations are needed to distinguish further substructure.

[3] The IRAS data were obtained using the IRAS data base server of the Space Research Organisation of the Netherlands (SRON) and the Dutch Expertise Centre for Astronomical Data Processing funded by the Netherlands Organisation for Scientific Research (NWO). The IRAS data base server project was also partly funded through the Air Force Office of Scientific Research, grants AFOSR 86-0140 and AFOSR 89-0320.

4. Results

4.1. Integrated line maps

Fig. 5a-h show our line mapping results of the total integrated intensities. All maps are presented over the same coordinate range for a better comparison, even though the higher excitation lines do not cover the full area. The [0,0] position of the maps refers to

$$\mathrm{RA}(1950) = 06^{\mathrm{h}}\ 38^{\mathrm{m}}\ 25^{\mathrm{s}},\ \mathrm{Dec}(1950) = 09^{\circ}\ 32'\ 25''.$$

IRS1 is located at RA(1950) = $06^{\mathrm{h}}\ 38^{\mathrm{m}}\ 24.9^{\mathrm{s}}$ and Dec(1950) = $09^{\circ}\ 32'\ 29''$ (Allen 1972, Allen et al. 1977). The small crosses in the contour plots indicate the measured positions. We have not fully sampled the maps, except for the central $40''\times40''$ part. In all line maps, our main beam temperatures peak at the [0,0] position.

In Fig. 5a and b we present contour plots of the total integrated line intensity of the $C^{18}O$ 2→1 transition with the JCMT and the IRAM telescopes. Both maps show IRS1 embedded in a more elongated cloud clump $\sim 1'$ in extent. Additionally, the $C^{18}O$ maps suggest less emission in the direction southwest of IRS1. This result is similar to the CO measurements by Phillips et al. (1988) and Phillips & Mampaso (1991). The lower CS transitions 2→1 and 3→2 (Fig. 5c and d) as well as the $C^{18}O$ 2→1

line measured by IRAM clearly show a second cloud clump around the small star cluster at the southeastern side of IRS1. The existence of such a southeastern clump is consistent with the continuum mapping results at 350, 450, 800, and 1300 μm by Ward-Thompson et al. (1996). The CS 5→4 map (Fig. 5e) also indicates an elongated cloud structure which is in good agreement with the CS 3→2 mapping results by Schwartz et al. (1985). The contour plot of the CS 7→6 line is shown in Fig. 5f. We mapped CS 7→6 only around the IRS1 position. This map indicates that IRS1 is embedded in a small dense clump. The peak in the intensity to the west was checked with repeated observations. In order to constrain the density of the clump at the position of the small star cluster, we measured a point strip across the cluster direction. The total integrated line intensity map as measured by the CO 3→2 line also suggests a more elongated cloud (Fig. 5g) but the spectra show very deep absorption.

The mapping result of the two blended methanol transitions $J = 5_2 \rightarrow 4_2$ and $J = 5_{-2} \rightarrow 4_{-2}$ is presented in Fig. 5h. This map clearly shows a different cloud structure from the other lines. We see two peaks: one to the north of IRS1 and one centered on the small star cluster to the south of IRS1 found in the K-band image. The peak to the north of IRS1 may trace the inner dense parts of the outflow streams. We also mapped the $J = 5_1 \rightarrow 4_1$ transition, for which the intensity is weaker than that of the two blended lines, and this map gives the same result.

4.2. The outflow

We investigated our observed spectra for line wings. The CS 3→2 and 2→1 as well as the CO 3→2 spectra possess noticeable wing emission. Moreover, we clearly found line wings in the CS 5→4 lines. In principle, the wing mapping gives the same results for all these lines. The higher spatial resolution compared with the earlier work of Phillips et al. (1988) and Phillips & Mampaso (1991) allows us to determine the outflow structure in much more detail.

In Fig. 6, we present the densest outflow parts: the mapped CS 5→4 wings overlayed with the K-band image. It is interesting to see that this map (like the other wing maps) shows two bipolar flows, one around IRS1 and one centered at the small star cluster.

The orientation of the outflow lobes around IRS1 seems to be located in the direction of the line of sight, but the lobes are displaced to the north in the same way as the methanol clump associated with IRS1 and the jet-like feature seen optically. Perhaps there is a wind driven by a southern source (W 178 or Cone Nebula's head ?) which pushed and compressed the southern side of the molecular cloud, as is also seen in the $C^{18}O$ map. This wind could have deformed the linear jet structure and bent the lobes to the northern side of IRS1. The direction of the infrared jet of IRS1 fits well into this scenario. The jet-flow angle would be very close to our line of sight. A possible opposite optical jet seems to be obscured by the source IRS1 itself.

The second flow to the southeastern side of IRS1 appears to have a different orientation with a larger angle to our line

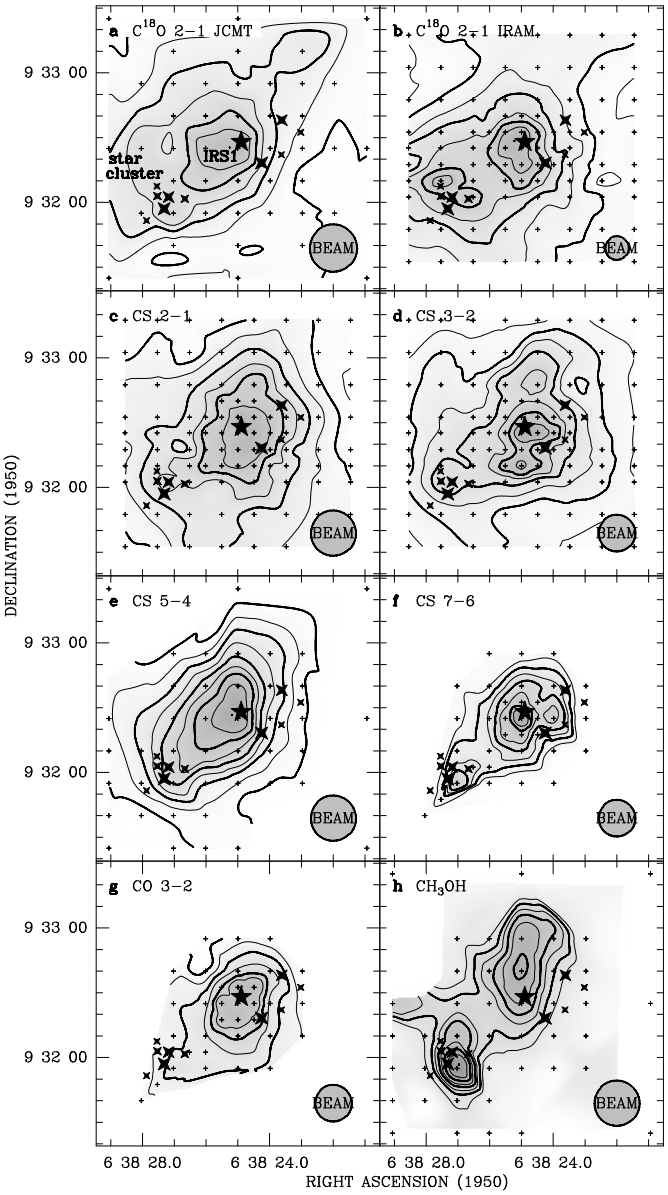

Fig. 5a–h. Contour plot of **a** the total $C^{18}O$ 2→1 emission in the velocity range +4.5 to +11 km s^{-1} measured at JCMT (peak value = 24.0 K km s^{-1}); **b** the total $C^{18}O$ 2→1 emission in the velocity range +5 to +11 km s^{-1} measured at IRAM (peak value = 31.3 K km s^{-1}); **c** the total CS 2→1 emission in the velocity range +5 to +11 km s^{-1} (peak value = 46.8 K km s^{-1}); **d** the total CS 3→2 emission in the velocity range +5 to +11 km s^{-1} (peak value = 48.8 K km s^{-1}); **e** the total CS 5→4 emission in the velocity range +3 to +14 km s^{-1} (peak value = 29.0 K km s^{-1}); **f** the total CS 7→6 emission in the velocity range +5 to +11.5 km s^{-1} (peak value = 20.8 K km s^{-1}); **g** the total CO 3→2 emission in the velocity range +5 to +25 km s^{-1} (peak value = 305.6 K km s^{-1}); **h** the total integrated methanol emission of the blended lines $J = 5_2 \rightarrow 4_2$ and $J = 5_{-2} \rightarrow 4_{-2}$ (peak value 2.8 K km s^{-1}). The contours are 30 to 90% of the peak values in steps of 10%. The small crosses indicate the points of the measurements. The positions of possible embedded star candidates found in the K-image are indicated with 4-toothed stars. IRS1 is shown by the 5-toothed star near the centre of the figure.

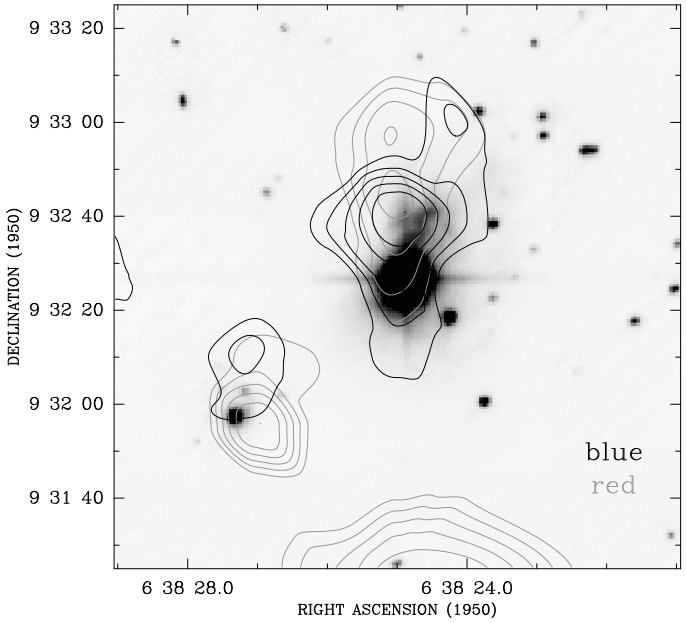

Fig. 6. Overlay of the contour plots of the red and the blue CS 5→4 line wing emission with the K-band image. The contours of the line emission are 50 to 90% of the peak values in steps of 10%. (peak values: red: 3.06 K km s^{-1}, blue: 3.13 K km s^{-1}) IRS1 clearly shows a jet-like feature. The small star cluster seems to drive the second outflow.

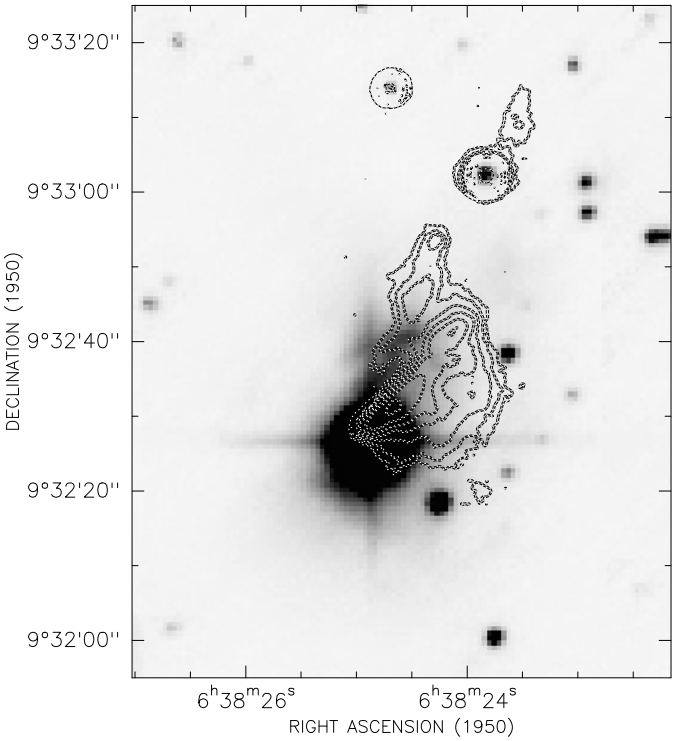

Fig. 7. Overlay of our K-band image (grey scale plot) with the R-band intensity contours (dotted lines) adopted from Scarrott & Warren-Smith (1989).

of sight. We do not have enough observational points around this area to get more detailed information about the extended structure of this flow. The small star cluster on the southeastern side of IRS1, perhaps the brightest member, seems to drive this flow.

As discussed in the introduction, there was some controversy in the literature about the outflow activities in the region around IRS1. Part of the discrepancy stems from the fact that high spatial resolution is essential to distinguish the two flows found here. Our flow structure divides the big red outflow lobe of Phillips & Mampaso (1991) into two separate flows whereas the results for the blue flows are quite similar. A clear shift of the blue lobe to the western side of IRS1 as mentioned by Phillips & Mampaso, could not be verified.

Our mapped line wing results imply that we see IRS1 nearly "pole on". This geometry was also proposed by Chini et al. (1986) based on their modeling of the continuum flux distribution. It explains why the infrared source is very bright, even though it is surrounded and still embedded in hundreds of magnitudes of extinction. A similar situation probably applies to other bright infrared sources, such as GL 2591 IRS1 and W 3 IRS5.

It is interesting to compare the images in the R and I bands as well as the polarization pattern in the R band measured by Scarrott & Warren-Smith (1989). They found an optical nebulosity associated with IRS1. The authors proposed that this nebula is not a simple reflection nebula illuminated by IRS1, but that it is the first visible part of a rim of a cavity created by the outflow. If we overlay our K image with the R- and I-band results by Scarrott & Warren-Smith (1989) (Fig. 7), the optical jet-like feature looks like the continuation of the infrared "wiggly" jet which is piercing the darker foreground cloud covering the largest part of the cavity. A possible jet-feature on the opposite site would be covered by the dark cloud.

4.3. Velocity structure

In Fig. 8, we present an overlay of the spectra of (from top to bottom) CO 3→2, C^{18}O 2→1, CS 5→4, and CS 7→6 around IRS1 with a spacing of 15″. We cut the top of the CO spectra because they are contaminated with the emission at the off-position. For these data, we used a quite close off-position to reduce the "moving" time of the telescope, since we were primarily interested in the CS 7→6 line in the opposite sideband. The C^{18}O 2→1 spectra were multiplied by a factor of 1.5. Fig. 9 displays a selection of spectra measured with IRAM (CS 2→1 plotted on top of CS 3→2 and C^{18}O 2→1).

In principle, we find similar line profiles as the IRAM measurements of CO isotopes by Krügel et al. (1987), which have comparable resolution to our measurements. Most of our CS and C^{18}O spectra of low optical depth (mainly CS 7→6, 5→4, and C^{18}O 2→1; see Sect. 5.2 for a discussion of optical depth) are not reproducable with a single Gaussian line. Krügel et al. (1987, 1989) concluded that IRS1 is located in a complex of subclouds embedded in an envelope of lower density. Especially the gas region around the small star cluster seems to have two clearly

Table 1. Parameters of observed lines at the IRS1 position.

Mol.	transition	ν (MHz)	$T_{\rm mb}$ [K]	rms [K]	ΔV [km·s^{-1}]	$\int T_{\rm mb}$dV [K·km·s^{-1}]	telescope/date
CS	10→ 9	489751.0	≤2.44	1.22	-	-	JCMT/Feb94
	7 → 6	342883.3	7.21[1]	0.29	2.7	20.6	JCMT/Feb94
	5 → 4	244935.6	8.48	0.21	3.3	30.0	JCMT/Feb94
	3 → 2	146969.0	14.4	0.35	3.8	43.8	IRAM/May95
	2 → 1	97981.0	11.6	0.11	4.1	42.2	IRAM/May95
^{13}CS	5 → 4	231221.0	0.32	0.04	1.7	0.59	JCMT/Apr94
C^{34}S	10 → 9	481916.1	≤2.44	1.22	-	-	JCMT/Feb94
	7 → 6	337396.6	≤0.84	0.42	-	-	JCMT/Feb94
	7 → 6	337396.6	0.48[2]	0.13	4.3	2.18	JCMT/Dec95
	5 → 4	241016.2	0.53	0.14	2.5	1.42	JCMT/Feb94
	3 → 2	144617.1	1.58	0.11	3.2	5.42	IRAM/Oct95
CO	4 → 3	461040.8	54.3	3.80	10.1	586	JCMT/Feb94
	3 → 2	345330.5	23.5	0.25	14.1	353	JCMT/Feb94
C^{18}O	2 → 1	219560.3	6.74	0.24	3.0	21.1	JCMT/Feb94
	2 → 1	219560.3	11.5	0.50	2.7	33.3	IRAM/May95
C^{17}O	3 → 2	337061.1	2.00	0.14	2.6	5.57	JCMT/Dec95
CH_3OH	$7_1 \rightarrow 6_1$ E$^+$	338615.0	0.26	0.12	7.5	2.08	JCMT/Dec95
	$7_6 \rightarrow 6_6$ E &	338404.5	1.83	0.12	4.9	9.57	JCMT/Dec95
	$7_0 \rightarrow 6_0$ A$^+$	338408.6					
	$7_{-1} \rightarrow 6_{-1}$ E$^-$	338344.6	1.40	0.12	5.1	7.59	JCMT/Dec95
	$7_3 \rightarrow 6_3$ A$^+$&	338540.7	0.36	0.12	3.1	1.19	JCMT/Dec95
	$7_3 \rightarrow 6_3$ A$^-$	338543.7					
	$7_2 \rightarrow 6_2$ E &	338721.6	0.52	0.12	3.6	2.02	JCMT/Dec95
	$7_{-2} \rightarrow 6_{-2}$ E	338722.9					
	$7_1 \rightarrow 6_1$ A$^-$	341415.5	0.51	0.12	3.5	1.88	JCMT/Dec95
	$5_2 \rightarrow 4_2$ E$^+$ &	241904.4	0.73	0.21	2.5	2.27	JCMT/Feb94
	$5_{-2} \rightarrow 4_{-2}$ E$^-$	241904.1					
	$5_2 \rightarrow 4_2$ E$^+$ &	241904.4	0.77	0.06	3.5	2.84	JCMT/Oct95
	$5_{-2} \rightarrow 4_{-2}$ E$^-$	241904.1					
	$5_2 \rightarrow 4_2$ A$^+$	241887.7	0.12	0.06	2.7	0.35	JCMT/Oct95
	$5_1 \rightarrow 4_1$ E$^+$	241879.1	1.69	0.06	3.2	1.69	JCMT/Oct95
	$5_0 \rightarrow 4_0$ A$^+$	241791.4	3.06	0.06	3.7	12.0	JCMT/Oct95
	$5_{-1} \rightarrow 4_{-1}$ E	241767.2	2.56	0.06	3.7	10.0	JCMT/Oct95
	$5_0 \rightarrow 4_0$ E	241700.2	0.94	0.06	3.0	3.02	JCMT/Oct95
	$5_1 \rightarrow 4_1$ E$^+$	241879.1	0.47	0.21	2.7	1.36	JCMT/Feb94
	$4_2 \rightarrow 3_1$ E$^+$	218440.0	1.12	0.06	3.1	3.79	JCMT/Oct95
	$4_2 \rightarrow 3_1$ E$^+$	218440.0	1.13	0.34	3.2	3.80	IRAM/Oct95
	$2_1 \rightarrow 1_0$ E$^+$	261805.7	0.36	0.09	4.2	1.63	JCMT/Oct95
CH_3CN	5 → 4 K=0	91987.0	0.32	0.11	1.8	0.62	IRAM/Oct95
	5 → 4 K=1	91985.3	0.23	0.11	2.3	0.57	IRAM/Oct95
	5 → 4 K=2	91980.0	0.19	0.11	2.3	0.47	IRAM/Oct95
	5 → 4 K=3	91971.1	≤0.22	0.11	-	-	IRAM/Oct95
	5 → 4 K=4	91958.7	≤0.22	0.11	-	-	IRAM/Oct95
H_2CO	$7_{1,7} \rightarrow 6_{1,6}$	491968.4	2.83	1.51	2.3	7.9	JCMT/Feb94
	$3_{0,3} \rightarrow 2_{0,2}$	218222.2	5.04	0.06	3.4	19.0	JCMT/Oct95
	$3_{0,3} \rightarrow 2_{0,2}$	218222.2	6.91	0.34	3.3	24.0	IRAM/Oct95
	$3_{2,2} \rightarrow 2_{2,1}$	218475.6	1.35	0.06	3.3	4.76	JCMT/Oct95
	$3_{2,2} \rightarrow 2_{2,1}$	218475.6	1.17	0.34	3.1	3.88	IRAM/Oct95
	$2_{1,1} \rightarrow 1_{1,0}$	150498.3	6.22	0.15	4.5	30.2	IRAM/Oct95
HDO	$1_{1,1} \rightarrow 0_{0,0}$	464927.5	≤1.94	0.97	-	-	JCMT/Feb94
H^{13}CN	3 → 2	259011.8	1.11	0.07	2.7	3.16	JCMT/Oct95
HC_3N	24 → 23	218324.8	0.38	0.06	2.4	1.00	JCMT/Oct95
[C I]	$^3P_1 \rightarrow ^3P_0$	492160.7	20.6	1.51	4.5	98.9	JCMT/Feb94

[1] average value for the [0,0] position of several measurements in 1994 and 1995
[2] C^{34}S 7→6 is blended with CN 340019.6 in the other sideband

Table 1. (continued)

Molecule (1)	transition (2)	ν (MHz) (3)	T_{mb} [K] (4)	rms [K] (5)	ΔV [km·s^{-1}] (6)	$\int T_{mb} dV$ [K·km·s^{-1}] (7)	telescope/date (8)
C_2H	$3,\frac{7}{2},4 \rightarrow 2,\frac{5}{2},3$	262004.3	2.93	0.05	1.9	5.92	JCMT/Oct95
	$3,\frac{7}{2},3 \rightarrow 2,\frac{5}{2},2$	262006.5	2.95	0.05	2.9	9.25	JCMT/Oct95
	$3,\frac{5}{2},3 \rightarrow 2\frac{5}{2},3$	262208.6	0.38	0.05	2.6	1.07	JCMT/Oct95
	$3,\frac{5}{2},3 \rightarrow 2\frac{3}{2},2$	262065.0	2.59	0.05	1.9	5.42	JCMT/Oct95
	$3,\frac{5}{2},2 \rightarrow 2\frac{3}{2},1$	262067.5	1.98	0.05	2.8	6.04	JCMT/Oct95
	$3,\frac{5}{2},2 \rightarrow 2\frac{3}{2},2$	262078.9	0.42	0.05	2.5	1.13	JCMT/Oct95
CN	$3\frac{5}{2}\frac{5}{2} \rightarrow 2\frac{3}{2}\frac{5}{2}$	340008.1	0.49	0.13	2.3	1.20	JCMT/Dec95
	$3\frac{5}{2}\frac{3}{2} \rightarrow 2\frac{3}{2}\frac{3}{2}$	340019.6	0.48[3]	0.13	4.3	2.18	JCMT/Dec95
	$3\frac{5}{2}\frac{7}{2} \rightarrow 2\frac{3}{2}\frac{3}{2}$	340031.5	2.50	0.13	2.2	5.97	JCMT/Dec95
	$3\frac{5}{2}\frac{3/5}{2} \rightarrow 2\frac{3}{2}\frac{1/3}{2}$	340035.4	2.10	0.13	2.8	6.32	JCMT/Dec95
	$3\frac{7}{2}\frac{7/9/5}{2} \rightarrow 2\frac{5}{2}\frac{5/7/3}{2}$	340248.6	4.58	0.13	3.0	14.7	JCMT/Dec95
	$3\frac{7}{2}\frac{5}{2} \rightarrow 2\frac{5}{2}\frac{5}{2}$	340261.8	0.57	0.13	1.2	0.76	JCMT/Dec95
	$3\frac{7}{2}\frac{7}{2} \rightarrow 2\frac{5}{2}\frac{7}{2}$	340265.0	0.63	0.13	2.6	5.57	JCMT/Dec95
SO	$7_6 \rightarrow 6_5$	261843.7	1.30	0.09	3.7	5.18	JCMT/Oct95
SO_2	$11_{3,9} \rightarrow 11_{2,10}$	262256.9	0.22	0.08	1.8	0.44	JCMT/Oct95
	$5_{2,4} \rightarrow 4_{1,3}$	241615.7	0.16	0.06	1.9	0.32	JCMT/Oct95
SiO	$6 \rightarrow 5$	260518.0	0.12	0.06	11.3	1.40	JCMT/Oct95[3]
			0.14	0.06	1.1	0.17	JCMT/Oct95
	$5 \rightarrow 4$	217104.9	0.63	0.30	5.7	3.83	IRAM/Oct95[3]
DCO^+	$3 \rightarrow 2$	216112.6	0.42	0.11	3.2	1.4	JCMT/Feb94
HCS^+	$6 \rightarrow 5$	256027.8	0.26	0.09	2.4	0.69	JCMT/Feb94
	$8 \rightarrow 7$	341350.8	0.14	0.12	2.7	0.43	JCMT/Dec95
HCO^+	$4 \rightarrow 3$	356734.3	13.6	0.56	4.1	59.3	JCMT/Feb94
$H^{13}CO^+$	$4 \rightarrow 3$	346993.4	0.96	0.23	2.5	2.1	JCMT/Feb94
	$3 \rightarrow 2$	260255.5	1.34	0.15	2.8	4.00	JCMT/Feb94
	$3 \rightarrow 2$	260255.5	1.61	0.14	2.5	4.44	JCMT/Oct95
	$1 \rightarrow 0$	86754.3	2.17	0.10	2.6	5.90	IRAM/Oct95
N_2H^+	$5 \rightarrow 4$	465824.8	4.11	0.75	2.5	10.9	JCMT/Feb94
N_2D^+	$3 \rightarrow 2$	231321.7	0.11	0.04	1.5	0.17	JCMT/Apr94

[3] only the Gaussian fit of the narrow line component

separated velocity components. These components, which are already seen in the DCO^+ data of Guélin et al. (1982) and which are also present in methanol, are located at the LSR-velocity of 6.3 and 8.2 km s^{-1} (Gaussian fits at the [+37.5,−37.5] position, see Fig. 9). For the lower CS transitions, it is not possible to distinguish the two velocity components at the cluster position because of the very deep self-absorption features. These CS spectra suggest that most of the emission of the main cloud component (V_{LSR} = 8.2 km s^{-1}) is absorbed, and Gaussian fits to their profiles to get approximate line intensities are hopeless. In order to determine whether the small cluster is associated with this second cloud component, we investigated the velocity structure of the optically thin $C^{18}O$ emission with channel maps. These maps indicate an association of gas with velocities between 5.5 and 7 km s^{-1} with the star cluster (Fig. 10) whereas gas with velocities between 8 and 10 km s^{-1} is located at the position of IRS1. We find the same result also for CS 3→2 and 2→1.

On the other hand, the spectra presented in Fig. 8 and 9 show a clear difference between the "subcloud components" in the velocity range V_{LSR} = 6 - 10 km s^{-1} and the broader line wings which are much weaker in the intensity. Thus, we can separate the outflow emission and the emission from the "low velocity subcloud components". Our presentation of the wing mapping is therefore not contaminated by "subcloud" emission.

In the mapped area, we do not find any systematic velocity trends around IRS1. If we assume that our proposed direction of the outflow along the line of sight is correct, then a possible disk-like structure would be perpendicular to the outflow direction, so that we cannot see any systematic velocity trends of detectable gas even though the disk-like structure is seen "face on".

4.4. Other species

In addition to CS and CO, we also searched for various other species at the [0,0] position. The results are summarized in Table 1. Some of these lines, in particular those of ions given in

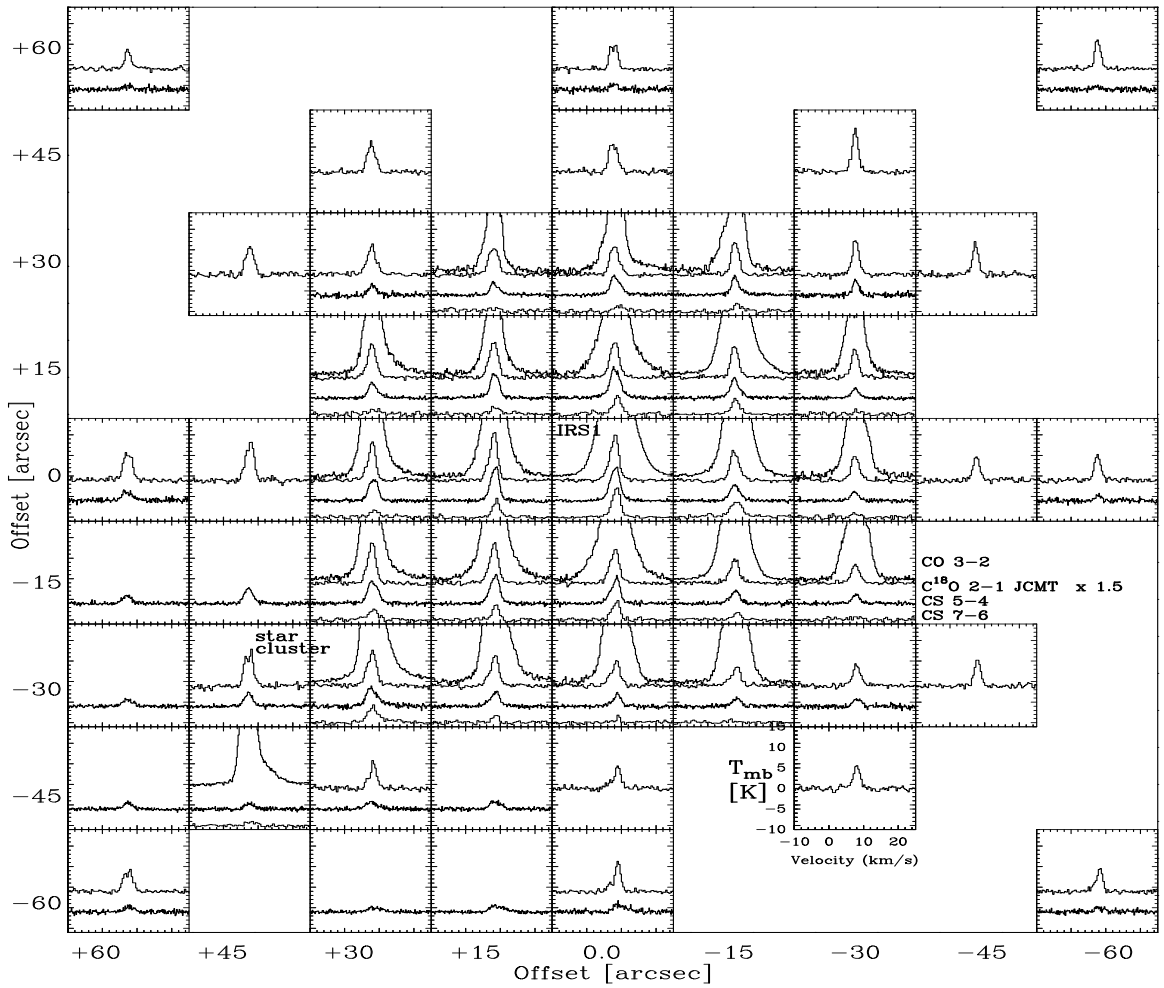

Fig. 8. Overlay of the CO 3→2, $C^{18}O$ 2→1 (multiplied by a factor of 1.5 for presentation), CS 5→4, and CS 7→6 spectra (from top to bottom) at some selected positions around IRS1. These lines were measured with the JCMT.

the second part of the table, are discussed in more detail by de Boisanger et al. (1996). Most of the lines are reproducable with single Gaussian profiles. Clear exceptions are SiO 6→5 and $C^{34}S$ 3→2. These lines show a very broad velocity component merged with a second narrow component. Fig. 11 shows examples of these spectra.

5. Analysis

In order to determine the physical parameters, especially the distribution of the temperature and the density, we performed statistical equilibrium excitation calculations to fit our observations, using an escape probability for the radiative transfer.

The applied method is described in more detail by Jansen et al. (1994). This code considers a homogeneous cloud medium without any assumption about the cloud geometry or systematic velocity fields and produces peak and integrated Gaussian line intensities. Since the line widths for different transitions of a species are fairly consistent, we used the main-beam temperatures for comparing the model results.

Since NGC 2264 is a dense cloud, we used only molecular hydrogen as a collision partner in all models. We do not include collisional (de)excitation with atomic hydrogen, helium, and free electrons. The cosmic background field represented by a blackbody with $T_{\rm bg}$ = 2.735 K was taken into account.

5.1. Temperature

In this section, we first present temperature estimates at the [0,0] position and subsequently discuss temperature constraints at some other positions around the IRS1 source.

The optically thick lines of the ^{12}CO molecule provide a lower limit on the temperature. The main beam temperature $T_{\rm mb}$ is related to the excitation temperature $T_{\rm ex}$ by

$$T_{\rm mb} = \eta_{\rm c} \frac{c^2}{2k\nu^2} \left[B_\nu(T_{\rm ex}) - B_\nu(T_{\rm bg})\right]\left(1 - e^{-\tau}\right), \quad (1)$$

where $B_\nu(T)$ is the Planck function, k is the Boltzmann's constant, ν is the frequency, and $\eta_{\rm c}$ indicates the beam filling factor of the source and is defined by the quotient of the solid angles

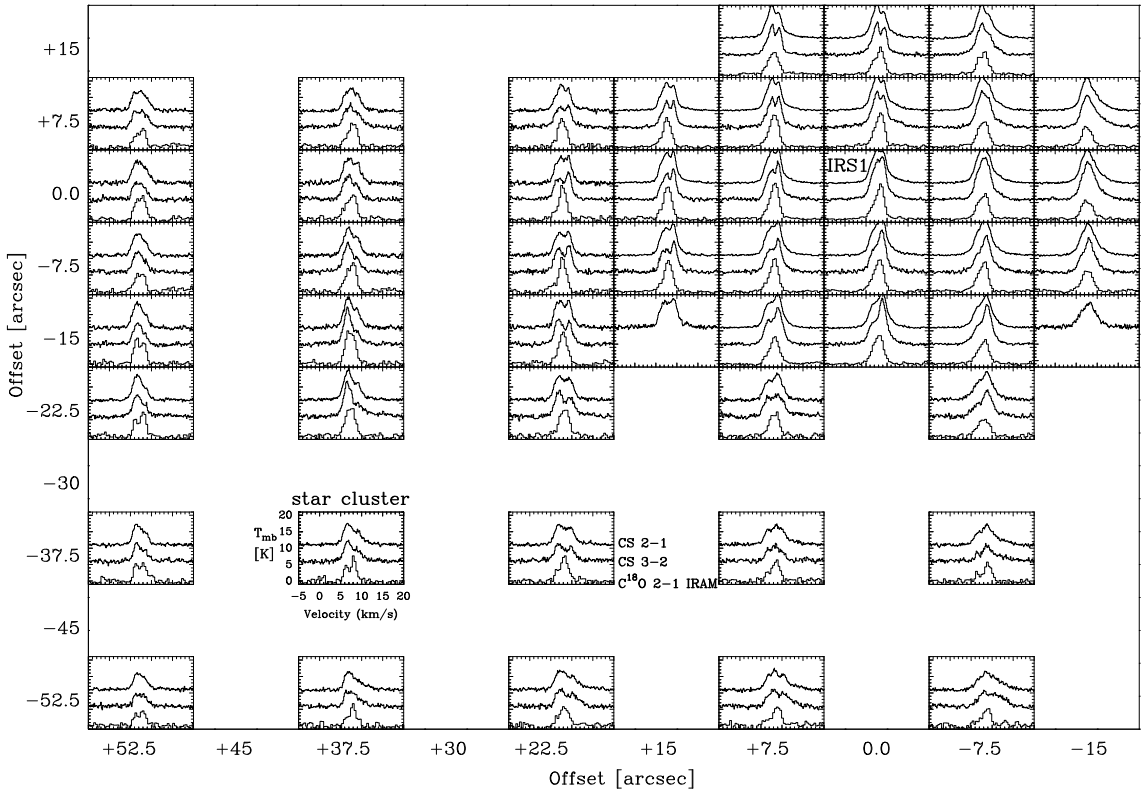

Fig. 9. Overlay of the CS 2→1, CS 3→2 and $C^{18}O$ 2→1 spectra (from top to bottom) at some selected positions around IRS1. These lines were measured with IRAM.

of the source and the source plus main beam. If the lines are highly optically thick ($\tau \gg 1$), the derived $T_{\rm mb}$ is of the order of $T_{\rm ex}$. To determine the peak $T_{\rm mb}$ for the ^{12}CO lines, we applied a mask on the spectra to cover the central absorption features resulting from emission at the off-position and from the self-absorption. The remaining part of the line profile is sufficient to reliably fit a Gaussian and determine the peak temperature to better than 10%. At the [0,0] position, we find excitation temperatures of $T_{\rm ex} \approx 40(\pm5)$ K from the CO 3→2 line and of $T_{\rm ex} \approx 64(\pm8)$ K from CO 4→3 which give a lower limit on the kinetic temperature. Here, we assumed a beam filling factor η_c = 1. Detailed excitation calculations do not reproduce the measured line strength ratio of CO 4→3/3→2 with a single temperature. The calculations suggest an optical depth of $\tau \gg 5$ for CO 3→2.

Additional constraints on the temperature at the [0,0] position can be obtained from excitation calculations of the H_2CO molecule. De Boisanger et al. (1996) used the $J = 3_{0,3} \rightarrow 2_{0,2}$ and $J = 3_{2,2} \rightarrow 2_{2,1}$ line ratios observed with the CSO and obtained $55(^{+10}_{-5})$ K in a 30″ beam. Repeated observations with the JCMT give a somewhat higher temperature of about $80(^{+5}_{-10})$ K in a 20″ beam. These values agree well with the temperature estimate obtained from our higher CO transitions as well as with earlier measurements by Krügel et al. (1987, 1989) in NH_3(4,4) (beamsize 40″) and CO 7→6 (beamsize 98″), which implied a small cloud component close to IRS1 with a temperature of 60 K.

Finally, we used the CH_3OH molecule to constrain the temperature. If we assume that the line emission is optically thin and the level populations are in LTE the excitation of the methanol molecule can be characterized by a single rotational temperature $T_{\rm rot}$. In this case, the relation between the integrated line intensity, column density and temperature is given by

$$\frac{N_{\rm u}}{g_{\rm u}} = \frac{3kc}{8\pi^3\mu^2\nu^2 S}\int T_{\rm mb}dv = \frac{N_{\rm tot}}{Q(T_{\rm rot})}e^{-E_{\rm u}/kT_{\rm rot}}, \quad (2)$$

where μ and S are the permanent dipole moment and the intrinsic line strength, and $N_{\rm u}$ and $g_{\rm u}$ are the column density and the degeneracy of the upper transition state. $N_{\rm tot}$ is the total column density, $Q(T_{\rm rot})$ is the rotational partition function at the temperature $T_{\rm rot}$, and $E_{\rm u}$ is the energy of the upper level of the transition. In order to produce the rotation diagram, we used the JPL spectral line catalog (Poynter & Pickett 1984, Groesbeck 1994). The least-squares fit value of the data points of the rotation diagram gives a rotational temperature of 27±3 K (Fig. 12). The scatter suggests that the level population distribution is not thermalized but still provides a lower limit to the kinetic temperature.

Although the CO 3→2 line gives a somewhat lower temperature at the [0,0] position than the CO 4→3 line, the mapped CO 3→2 line provides some more information about the temperature behaviour around IRS1. The CO 3→2 intensities at

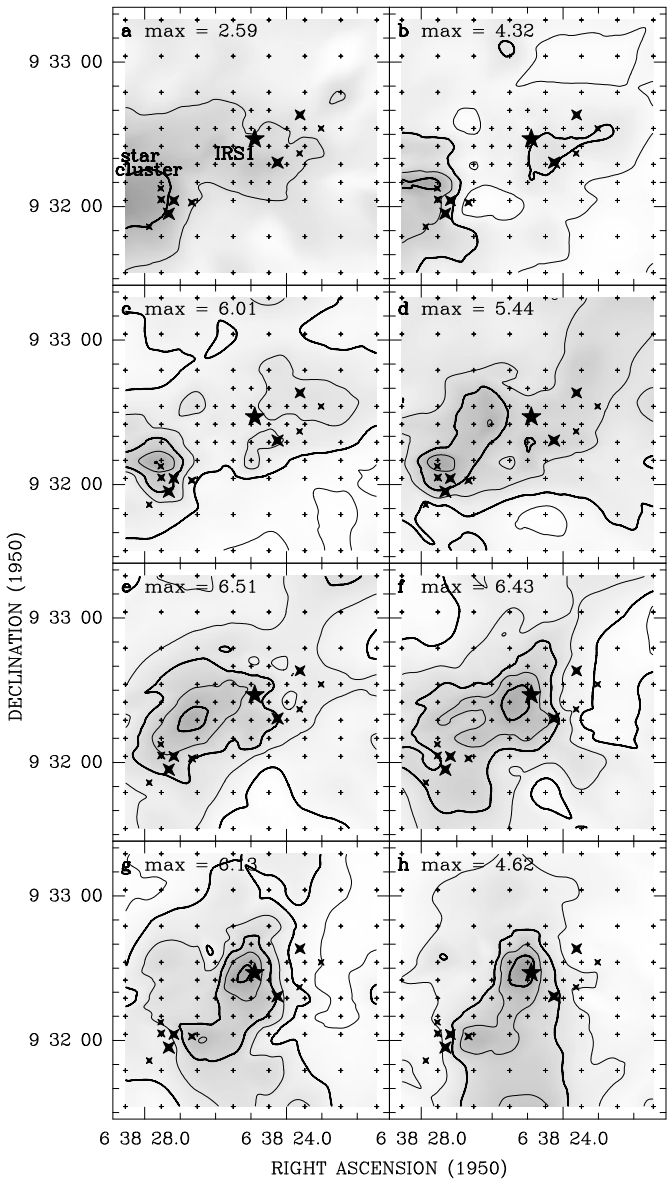

Fig. 10a–h. Channel maps of $C^{18}O$ 2→1 observations with IRAM. The contours are 1.0, 2.0, 3.0, 4.0, 5.0, 6.0 K km s^{-1}. The peak values (max) are given in K km s^{-1}. **a** 5.5<V_{LSR}<6.0 km s^{-1}, **b** 6.0<V_{LSR}<6.5 km s^{-1}, **c** 6.5<V_{LSR}<7.0 km s^{-1}, **d** 7.0<V_{LSR}<7.5 km s^{-1}, **e** 7.5<V_{LSR}<8.0 km s^{-1}, **f** 8.0<V_{LSR}<8.5 km s^{-1}, **g** 8.5<V_{LSR}<9.0 km s^{-1}, **h** 9.0<V_{LSR}<9.5 km s^{-1}.

the other map positions suggest no strong temperature decrease around IRS1 (typical temperature 20-30 K) with exception of the direction to the second clump. At the position of the small star cluster, the CO 3→2 line suggests a temperature of about 65 K. A scan across the small star cluster and IRS1 has been made in the H_2CO 218 GHz lines with the IRAM 30m telescope. At the position of the small cluster, these data give a temperature between 70 and 100 K, if we assume that the lines are optically thin. Furthermore, both the CO and H_2CO data at the position [+15,−15] imply a warmer "bridge" of gas between IRS1 and the small star cluster (T_{kin} = 60-70 K). The H_2CO IRAM measurement 15″ to the north of IRS1 suggests that an area of about 1′ × 1′ has a temperature of at least 50 K.

Our inferred temperature distribution agrees well with earlier determinations at lower spatial resolution. The map of CO intensities by Phillips et al. (1988) also shows a temperature enhancement at the position of the small star cluster. Various other observations by Krügel et al. (1987), Phillips et al. (1988), Phillips & Mampaso (1991), and Schreyer et al. (1996) reveal a temperature of about 25 K of the extended gas cloud around IRS1. Our CO 3→2 results coincide with this temperature if we average the values of our data points.

Based on all temperature estimates, we conclude that NGC 2264 IRS1 is located in a gas clump with a temperature of 55 K surrounded by more extended cloud material with a temperature of 20 to 30 K. Gas close to IRS1 seems to have a temperature higher than 55 K. Additionally, the small star cluster is located in a second warmer clump with a temperature of ≥70 K.

5.2. Density

To determine the density, we analyzed the observed line ratios with statistical equilibrium excitation calculations.

First, we investigated the density at the [0,0] position based on our JCMT observations. The analysis of the CS 7→6/5→4 line ratio resulted in a density of 3.2(±1.5) 10^6 cm^{-3} if we apply a temperature of 55 K. Calculations with a temperature of 80 K give an only slightly lower density of 2.1 10^6 cm^{-3}. This density value lies within the calibration errors of the observed line intensities. Density determinations using other molecules and ions (see for more details de Boisanger et al. 1996: e.g. H_2CO, N_2H^+, $H^{13}CO^+$) also give somewhat lower densities using a temperature of 55 K. Thus, we conclude that the beam-averaged density of the cloud centre is around $2(^{+2}_{-1})$ 10^6 cm^{-3}. The observed upper limit on the CS 10→9 intensity is in agreement with our derived density, and indicates that there is no significant fraction of even higher density gas in the 12″ JCMT beam.

To check the optical depth τ of the CS line centres at the [0,0] position, we measured the isotopic lines $C^{34}S$ 10→9, 7→6, and 5→4. Assuming a standard isotope ratio of $^{32}S/^{34}S$ of 22.5, we found that the CS 7→6 and 5→4 lines are only slightly optically thick ($\tau \approx 0.35$). The radiative transfer calculations give the same values for these CS lines at the [0,0] position, which indicates that the filling factor of the gas must be close to unity. The optical depths in the outer regions of IRS1 range between 0.08 and 0.02 for CS 7→6 and between 0.1 and 0.4 for CS 5→4 (Table 2). The small star cluster region shows an optical depth of ∼0.5 for both CS transitions.

In order to obtain a density distribution, we determined the densities with statistical equilibrium excitation calculations at selected positions around IRS1 where both the CS 7→6 and 5→4 lines were measured. We observed these lines on an inner grid with a point-spacing of 15″. Since the CS 7→6 map was obtained with a smaller beamsize than the 5→4 measurements, we convolved the 7→6 map to the same beamsize of 21″ as the 5→4 map. Based on our temperature estimates, we first assumed an uniform temperature of 55 K at all points. The temperature

Table 2. Fit results of the CS 7→6/5→4 line ratios for a uniform temperature of 55 K. All error estimates are displayed in brackets.

offset position x	y	n $\times 10^6$ [cm^{-3}]	N(CS) $\times 10^{13}$ [cm^{-2}]	$\tau_{CS7\to6}$	$\tau_{CS5\to4}$
(1)		(2)	(3)	(4)	(5)
+45	-45	$4.0(^{+5.0}_{-2.0})$	$1.2(^{+0.4}_{-0.2})$	0.49	0.48
+30	+15	$1.3(^{+1.5}_{-0.5})$	$4.1(^{+2.0}_{-1.5})$	0.14	0.30
+30	0	$1.2(^{+1.0}_{-0.8})$	$7.2(^{+5.0}_{-4.0})$	0.22	0.56
+30	-15	$1.6(^{+1.5}_{-1.2})$	$7.2(^{+5.0}_{-3.0})$	0.23	0.48
+30	-30	$6.5(^{+4.0}_{-1.0})$	$6.0(^{+0.5}_{-1.0})$	0.17	0.14
+15	+30	$1.4(^{+1.5}_{-0.7})$	$2.9(^{+2.0}_{-1.0})$	0.10	0.21
+15	+15	$1.7(^{+2.0}_{-1.0})$	$6.4(^{+5.0}_{-2.0})$	0.25	0.41
+15	0	$1.8(^{+3.0}_{-1.0})$	$8.6(^{+5.0}_{-3.0})$	0.38	0.56
+15	-15	$2.6(^{+3.0}_{-0.7})$	$7.1(^{+5.0}_{-2.0})$	0.30	0.39
+15	-30	$2.2(^{+2.5}_{-1.0})$	$3.4(^{+2.5}_{-1.0})$	0.13	0.18
0	+30	$0.97(^{+1.0}_{-0.7})$	$6.9(^{+5.0}_{-3.0})$	0.18	0.48
0	+15	$2.6(^{+4.0}_{-1.0})$	$7.7(^{+5.0}_{-2.0})$	0.29	0.35
0	0	$3.2(^{+5.0}_{-2.0})$	$8.4(\pm 2.0)$	0.34	0.35
0	-15	$3.6(^{+5.0}_{-2.0})$	$5.7(^{+3.0}_{-1.0})$	0.25	0.25
0	-30	$2.1(^{+2.0}_{-1.0})$	$2.9(^{+2.0}_{-1.0})$	0.13	0.19
-15	+30	$0.98(^{+1.5}_{-0.7})$	$6.0(^{+5.0}_{-3.0})$	0.18	0.17
-15	+15	$3.0(^{+5.0}_{-1.5})$	$4.3(^{+2.5}_{-1.0})$	0.19	0.21
-15	0	$7.7(^{+3.0}_{-2.0})$	$3.6(\pm 0.2)$	0.12	0.10
-15	-15	$5.7(\pm 3.0)$	$2.6(^{+0.7}_{-0.2})$	0.10	0.09
-30	+15	$2.9(^{+4.0}_{-1.5})$	$1.8(^{+1.0}_{-0.5})$	0.08	0.09
-30	0	$2.4(^{+2.5}_{-1.0})$	$1.7(^{+2.5}_{-0.5})$	0.08	0.10

structure is important in the analysis, since the J = 7 level of CS lies at 65 K above ground. The density map produced in this way differs from the integrated line emission maps of the CS transitions. The calculated density distribution is shown in Fig. 13, and the fits are listed in Table 2. This map shows a density enhancement to the (south-)western side of the infrared source, which is caused by the low line ratio measured at this position. Although the enhancement is barely significant within the uncertainties, we repeated the observations at this position and found the same result. The CS 7→6 map (Fig. 5f) gives some evidence for a small dense clump at this position, and the K-image shows further "embedded" low-mass stars on the western side of IRS1. In order to test whether this structure could be produced by small pointing differences between the 5→4 and 7→6 map, we shifted the maximum of the convolved 7→6 map by 3-5″ to the peak position of the 5→4 map. All resulting density distributions show a similar density structure.

We furthermore calculated the density distribution with the assumption of a spherical temperature gradient with $T(r) \sim r^{-1}$, where r is the distance from the [0,0] position. At the centre position, we assumed a temperature of 55 K, which drops to 30 K at r = 30″. The resulting density distribution gives higher values ($\geq 10^8$ cm^{-3}) in the outer regions than at the IRS1 position. This strongly suggests that the temperature is nearly constant over the considered area of 1′ × 1′ around IRS1. This conclusion is supported by the temperature estimates obtained from the formaldehyde measurements.

We also constrained the density at the position of the second star cluster by fits of the CS 7→6/5→4 ratio. The results imply a density of $6(^{+4}_{-1})$ 10^6 cm^{-3} at the map position [+30″,−30″] if we use a temperature of 55 K (see Fig. 13). Fits with a temperature of 80 K provide lower densities of about 4 10^6 cm^{-3}. Thus, the density at this position appears higher than at IRS1.

Additionally, we tried to fit the line ratios of the lower CS transition. We convolved the CS 5→4 and CS 3→2 lines to the beamsize (25″) of CS 2→1. However, the Gaussian fits (with masks) to constrain the line intensities and the line areas possess quite large errors caused by deep self-absorption features of these lines, especially in the region of the second small star cluster (see Fig. 9). Moreover, it was not possible to distinguish the two separate velocity components found in C^{18}O in the range of the small star cluster because the velocity difference is too small to fit single CS Gaussian lines. The result of the point by point density determination for the whole area gives lower densities than the CS 7→6/5→4 ratios. The calculations provided approximately the same density value of $3(\pm 2)$ 10^5 cm^{-3} at all points with the exception of the centre position where a density of $7(\pm 3)$ 10^5 cm^{-3} was found. The lower densities and the relatively high optical depths of the lower CS transitions (CS 3→2: $\tau \geq 1$) indicate that these lines originate from an outer cloud shell and do not trace the inner dense cloud core.

5.3. Column density and CS abundance

The application of the above mentioned radiative transfer code to fit the CS line intensities with a temperature of 55 K constrains the density and the column density values as input parameters. At the [0,0] position, N(CS) = $9(\pm 1.0)$ 10^{13} cm^{-2} is required to reproduce the absolute intensities, when an average central density of $2(^{+2}_{-1})$ 10^6 cm^{-3} is assumed. The column densities for all map positions estimated in terms of the convolved CS line ratios and an uniform gas temperature of 55 K in this region are summarized in Table 2. The error estimates are given in brackets, and are based on an assumed calibration uncertainty of 20% of the fitted line intensities.

To determine the total (beam-averaged) H_2 column densities, we used our JCMT C^{18}O measurements, which have the same beamsize as the CS 5→4 measurements. We fitted the C^{18}O intensities in terms of the same physical parameters (temperature and density) as obtained from the excitation analysis of the CS lines.

The C^{18}O 2→1 lines are mostly optically thin, although this is not completely certain at the position of the small star cluster. Fits of the C^{18}O 2→1 observations give optical depths between 0.01 and 0.16. In order to estimate the column density of H_2, we used the abundance ratios of CO/C^{18}O = 500 and the value of CO/H_2 = 1.7 10^{-4} which is discussed by de Boisanger et al. (1996) and corresponds to the lower limit found by Lacy et al. (1994) from infrared absorption line observations. For the average central density of $2(^{+2}_{-1})$ 10^6 cm^{-3}, we obtained an H_2 column density of $N(H_2)$ = 6.8 10^{22} cm^{-2} and a CS abundance with respect to H_2 of X(CS) = 1.3 10^{-9}. Fits of the C^{17}O 3→2 line obtained at the CSO applying the same CO/H_2 ratio and

Table 3. Fit results of the H_2 column densities and CS abundances. For the offset position [+45,−45], there are two velocity components indicated with (a) and (b): (a) V_{LSR} = 6.3 km s^{-1}, (b) V_{LSR} = 8.2 km s^{-1}.

offset position x	y		$\tau_{C^{18}O}$	$N(H_2)$ $\times 10^{22}$ [cm^{-2}]	X(CS) $\times 10^{-9}$
(1)			(2)	(3)	(4)
+45	-45	(a)	0.09	$1.5(\pm 0.3)$	$0.8(^{+0.6}_{-0.3})$
		(b)	0.14	$2.4(\pm 0.4)$	$0.5(^{+4.0}_{-2.0})$
+30	+15		0.11	$4.3(\pm 0.8)$	$1.0(^{+1.0}_{-0.5})$
+30	0		0.13	$4.6(\pm 1.0)$	$1.5(^{+4.0}_{-1.0})$
+30	-15		0.14	$5.1(\pm 1.0)$	$1.4(^{+2.0}_{-1.0})$
+30	-30		0.12	$5.3(\pm 1.0)$	$1.2(\pm 0.5)$
+15	+30		0.09	$4.2(^{+0.5}_{-0.8})$	$0.7(^{+1.0}_{-0.3})$
+15	+15		0.12	$5.0(\pm 1.0)$	$1.3(^{+3.0}_{-0.7})$
+15	0		0.17	$6.1(^{+1.2}_{-1.4})$	$1.4(^{+3.0}_{-0.8})$
+15	-15		0.14	$5.4(\pm 1.0)$	$1.3(^{+2.0}_{-0.8})$
+15	-30		0.10	$4.1(\pm 0.8)$	$0.8(^{+1.0}_{-0.3})$
0	+30		0.10	$4.0(^{+0.8}_{-1.1})$	$1.7(^{+3.0}_{-1.0})$
0	+15		0.12	$5.1(\pm 1.0)$	$1.5(^{+2.5}_{-0.7})$
0	0		0.16	$6.8(^{+0.8}_{-1.2})$	$1.2(^{+1.5}_{-0.5})$
0	-15		0.12	$5.2(\pm 1.0)$	$1.1(^{+1.5}_{-0.5})$
0	-30		0.09	$3.7(\pm 0.7)$	$0.8(^{+1.0}_{-0.3})$
-15	+30		0.12	$3.9(\pm 0.9)$	$1.5(^{+5.0}_{-1.0})$
-15	+15		0.11	$3.9(\pm 0.8)$	$1.1(^{+1.5}_{-0.5})$
-15	0		0.10	$4.3(\pm 0.8)$	$0.8(^{+0.6}_{-0.2})$
-15	-15		0.08	$3.5(\pm 0.7)$	$0.8(^{+0.5}_{-0.2})$
-30	+15		0.10	$3.1(\pm 0.6)$	$0.6(^{+0.6}_{-0.2})$
-30	0		0.08	$3.0(^{+0.1}_{-1.0})$	$0.6(^{+1.0}_{-0.2})$

the CO/C^{17}O ratio of 2600 (see de Boisanger et al. (1996) for more details) resulted in an H_2 column density of 8.3 10^{22} cm^{-2} and a CS abundance of 1.1 10^{-9}. Observations of the same line with the JCMT yielded a somewhat lower column density of 3.1 10^{15} cm^{-2}.

The variation of the total H_2 column density over the shown region in Fig. 13 can be constrained by the C^{18}O 2→1 data at the other map positions. The results are presented in Table 3. A typical value of $N(H_2)$ at the outer positions of the grid is $3(\pm 1)$ 10^{22} cm^{-2}. For these calculations, we fitted most of the C^{18}O lines surrounding the IRS1 position with a single Gaussian profile. Near the second star cluster, we can clearly distinguish two velocity components which are indicated with (a) (V_{LSR} = 6.3 km s^{-1}) and (b) (V_{LSR} = 8.2 km s^{-1}) in Table 3.

We computed the relative CS abundances X(CS) = N(CS)/$N(H_2)$ at all positions where beam-averaged values of N(CS) and $N(H_2)$ are obtained. The resulting values are shown in Table 3 and their spatial distribution is presented in Fig. 14. The errors are caused by assuming a calibration error of 20% for C^{18}O combined with the error estimated for N(CS).

The situation for determining the CS abundance near the second star cluster is more complicated. In contrast to C^{18}O, only a single broader line can be fitted in CS. A separation of the two velocity components is not possible. Thus, we can only derive a single value of the density at the position [+45,−45]. To obtain an approximate value for the CS abundance, we used the same density value for both C^{18}O line components.

Fig. 14 illustrates that we do not find any systematic trend in the (beam-averaged) abundance distribution. Small abundance variations are within the errors. The result implies a nearly constant abundance of about X(CS) = 1($\pm$0.5) 10^{-9} over the cloud. On the other hand, this result is not surprising because the whole region seems to have the same quite warm, uniform gas temperature. Therefore, no noticeable abundance gradient is expected. The inferred CS abundance is similar to that found in other star-forming regions (see Sect. 7).

5.4. Mass estimates

The gas mass of the cloud around IRS1 was estimated based on the $N(H_2)$ results obtained from the C^{18}O line intensity fits mentioned above. A mean H_2 column density was derived by averaging the values of the various offset positions. Using a circular area with a radius of $r = 30''$, which corresponds to the mapped area in CS 7→6, the mass within this field is 40 M$_\odot$. In order to constrain the H_2 column density at the outer map positions where no density estimates are available, we used the conversion of $N(H_2) = 3\times 10^{21} \int T_{mb} \Delta V$ (Frerking et al. 1982). The total mass within the mapped area ($2' \times 2'$) in C^{18}O is about 175 M$_\odot$. Using the virial theorem where $\alpha_{vir} = (1 - p/3)/(1 - 2p/5)$ and the density gradient $p = 2$, the virial mass M_{vir} can be computed by

$$M_{vir} = \frac{5}{\sqrt{8\ln 2}} \frac{R\,(\Delta V)^2}{\alpha_{vir} G} = 104\, \frac{2R[\mathrm{pc}]\,(\Delta V[\mathrm{km\ s^{-1}}])^2}{\alpha_{vir}} [M_\odot], \quad (3)$$

where G is the gravitational constant and R the radius of the cloud (Williams et al. 1994). We adopted R = 0.6 pc from the extension of the NH_3 (1,1) map by Krügel et al. (1987) where the density decreased to about 1 10^4 cm^{-3}. The mean line width of all C^{18}O and CS 7→6 lines is ΔV = 2.9 km s^{-1}. Applying these values, we find a total virial mass of M_{vir} = 630 M$_\odot$ for this cloud. All our mass estimates coincide well with the results reported by Krügel et al. (1987).

6. Chemistry

6.1. Column densities

In order to gain more insight into the chemistry of this region of intermediate-mass star formation, the beam-averaged abundances of the various species listed in Table 1 were calculated. For most molecules, the column densities were obtained from statistical equilibrium excitation calculations, in the same way as described by Helmich & van Dishoeck (1997) for the W 3 region. The average density of 2 10^6 cm^{-3} and a temperature of 55 K were used to fit the observed line strengths. For CH_3OH, the rotation diagram method was used, because of the lack of collisional rate coefficients.

Table 4. Column densities and relative abundances[a] of various species using n = 2 10^6 cm $^{-3}$, and $T_{\rm kin}$ = 55 K.

	N[cm^{-2}]	$X = N/N(H_2)$			
species	NGC 2264 IRS1	NGC 2264 IRS1	W 3 IRS4[b]	W 3 IRS5[b]	IRAS 16293-2422[c]
H_2	6.8 10^{22}	1.0	1.0	1.0	1.0
CO	1.1 10^{19}	1.7(-4)	2.8(-4)	2.8(-4)	1.0(-4)
CS	9.0 10^{13}	1.3(-9)	5.8(-9)	1.5(-9)	1.1(-9)
C	1.8 10^{18}	2.6(-5)		3.2(-5)	1.5(-6)
CN	1.1 10^{14}	1.6(-9)	4.8(-9)	1.4(-9)	1.0(-10)
HCN	2.2 10^{14}	3.2(-9)	1.2(-8)	4.0(-9)	1.9(-9)
HC_3N	1.6 10^{13}	2.4(-10)	<2.6(-10)	<7.6(-11)	2.5(-11)
NH_3	8.0 10^{14}[d]	1.2(-8)	...	...	1.0(-8)
C_2H	2.0 10^{14}	4.6(-9)	2.8(-9)	9.2(-10)	2.5(-10)
H_2CO	2.0 10^{14}	9.0(-10)	1.1(-9)	6.2(-10)	7.0(-10)
CH_3OH	6.0 10^{14}	8.8(-9)	6.0(-9)	1.2(-9)	4.4(-9)
CH_3CN	5.6 10^{12}	8.2(-11)	<1.7(-10)	<7.2(-11)	1.5(-10)
SO	6.2 10^{13}	9.2(-10)	2.0(-9)	3.8(-8)	3.9(-9)
SO_2	1.4 10^{13}	2.0(-10)	2.2(-9)	4.0(-8)	1.5(-9)
SiO	3.2 10^{12}	4.7(-11)	3.2(-10)	4.0(-11)	1.0(-10)
HCO^+	1.5 10^{14}	2.2(-9)	5.4(-9)	1.5(-9)	1.8(-9)
DCO^+	7.4 10^{11}	1.1(-11)	...	7.4(-12)	1.5(-11)
HCS^+	1.8 10^{12}	2.6(-11)	<2.8(-10)	4.8(-12)	2.0(-11)
N_2H^+	2.5 10^{13}	3.6(-10)	...	< 1.3(-12)	...
HDO	<7.1 10^{13}	<1.0(-9)	<4.3(-11)	<3(-11)	1.0(-8)

[a] $N(H_2)$ = 6.8 10^{22} cm^{-2}
[b] From Helmich & van Dishoeck (1997)
[c] From Blake et al. (1994) and van Dishoeck et al. (1995)
[d] From Schreyer et al. (1996) and Krügel et al. (1987) using NH_3(1,1), (2,2); the (4,4) line gives a factor of 4 lower column density

For the ions such as HCO^+, the inferred column densities are the same as found by de Boisanger et al. (1996). For H_2CO, the new JCMT data were used in the analysis, rather than the older CSO values. Most observed H_2CO lines belong to para-H_2CO, and indicate N(p-H_2CO) = 5.0 10^{13} cm^{-2}. For an ortho/para ratio of 3, this gives $N(H_2CO)$ = 2 10^{14} cm^{-2}.

For CH_3CN, only observations of the low-lying $5_K \rightarrow 4_K$ band obtained with IRAM are available. The lines are weak, but a separate analysis of ortho- and para-CH_3CN is possible. The resulting column densities of 2.6 10^{12} cm^{-2} and 3.0 10^{12} cm^{-2} indicate that the ortho/para ratio is close to the high-temperature value of unity. Note, however, that CH_3CN is often found to have a very compact distribution (e.g., Wink et al. 1994 for W 3(H_2O)), with highly optically thick lines. Interferometric observations are needed to determine whether this is also the case for NGC 2264. For CH_3OH, the rotation diagram method yields $T_{\rm rot}$ = 27 $\pm$ 3 K (see Sect. 5.1) and $N(CH_3OH)$ = 6.0 $\pm$ 1.6 10^{14} cm^{-2}.

The listed column density for HCN is derived from the optically thin $H^{13}CN$ lines, assuming $^{12}C/^{13}C$ = 60. A single line of the unsaturated molecule HC_3N has been observed, which gives a rather high column density of 1.6 10^{13} cm^{-2} in a 21″ beam.

Of the sulfur-oxides, only SO is clearly detected. In all the spectra, only two SO_2 lines have been found, of which one highly uncertain. Assuming $T_{\rm rot}$ = 20 K, similar to CH_3OH, a column density of 1.4 10^{13} cm^{-2} is found. However, this value should be regarded as an upper limit.

The SiO 6→5 line shows an unusual profile with two components: a narrow spike (ΔV < 1 km s^{-1}) on top of a broad component (see Fig. 10). Only the broad feature is taken into account in the analysis.

The resulting column densities are summarized in Table 4 and refer to the JCMT beam of 15-20″.

6.2. Abundances

In order to obtain the abundances $N(X)/N(H_2)$ listed in Table 4, an H_2 column density of 6.8 10^{22} cm^{-2} was applied as the reference (cf. Sect. 5.3). The resulting values are compared with those obtained in the high-mass star forming regions W 3 IRS 4 and IRS5, as well as the low-mass IRAS 16293-2422 object (Helmich & van Dishoeck 1997, Blake et al. 1994, van Dishoeck et al. 1995). It is important to note that the abundances for these regions were obtained using the same telescope(s) and the same methods of analysis. The main difference lies in the adopted CO/H_2 abundance ratio, which is nearly a factor of 3 higher in

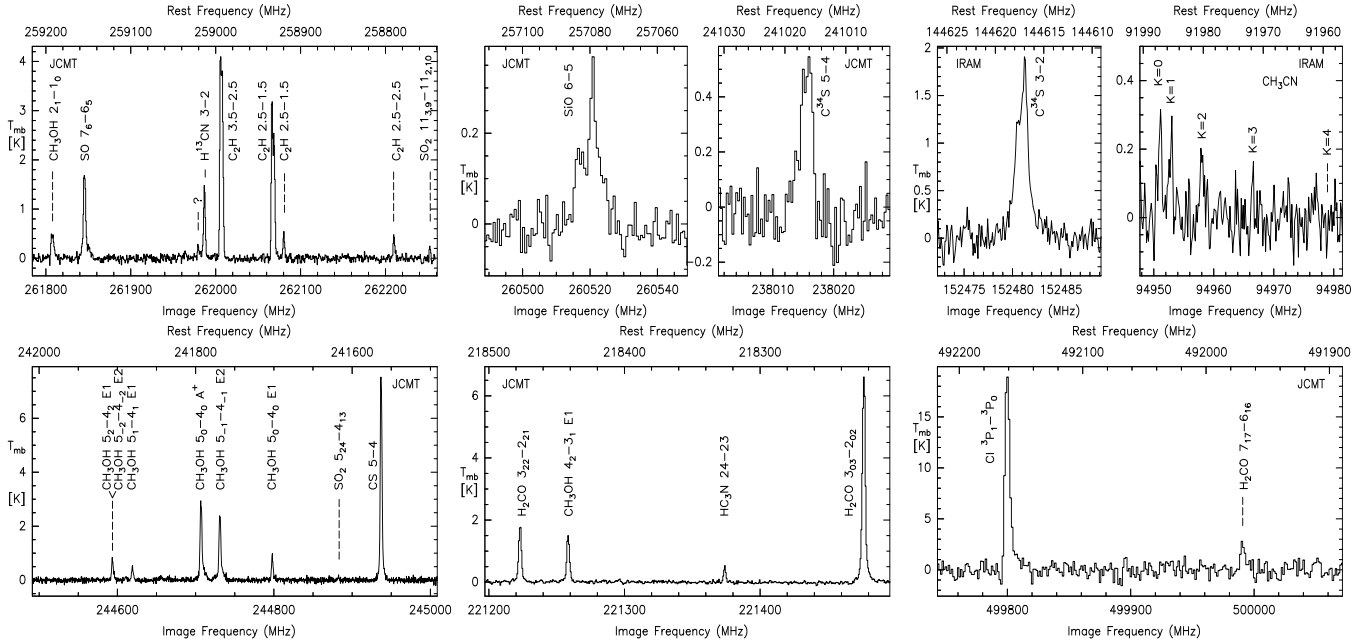

Fig. 11a–h. Examples of some spectra.

the W 3 cloud than in IRAS 16293. To bring all abundances to the same scale as for NGC 2264, the W 3 abundances need to be divided by a factor of 1.65, whereas the IRAS 16293 abundances need to be multiplied with a factor of 1.7. In general, it should be emphasized that all abundances derived here are averaged over 15-20″ beams, but that structure on much smaller scales is present. A more detailed chemical analysis must await higher spatial resolution observations and a more detailed physical model of the regions.

Within the uncertainties associated with the observations and analysis, a few obvious conclusions regarding the NGC 2264 chemistry can be drawn. First, the abundances of simple species such as CS and HCO^+ are similar within a factor of a few in the various regions. Second, the abundances of the organic molecules H_2CO and CH_3OH are somewhat enhanced, especially compared with W 3 IRS5, whereas the sulfur-bearing molecules SO and SO_2 are lacking in NGC 2264. The most striking aspect of the NGC 2264 chemistry is, however, its peculiar nitrogen chemistry, especially its very high N_2H^+ and inferred N_2 abundances (van Dishoeck et al. 1992; de Boisanger et al. 1996), and its large HC_3N abundance. On the other hand, the HCN, CN and NH_3 values appear similar to other regions.

In the chemical scenario described, e.g., in van Dishoeck & Blake (1995), the enhanced abundances of H_2CO and CH_3OH result from evaporation of grain mantles when the young star starts to heat up its surroundings. This leads to the "hot core" phase, in which complex organic molecules are readily formed (Charnley et al. 1992, Caselli et al. 1993). Some H_2O- and CO-ice is still present along the line of sight toward NGC 2264 (Tielens et al. 1991), but the temperatures in the vicinity of the YSO are high enough that evaporation of the more volatile species must have occurred. The return of the molecules to the gas phase can be aided by shocks: the CH_3OH maps in Fig. 5 clearly show that this species is associated with the outflow, as is also seen in other objects (Sandell et al. 1994, Bachiller et al. 1995, Bachiller 1997).

Sulfur-bearing species like SO and SO_2 are also often found to be associated with outflows. In W 3 IRS5, the abundances of these species are greatly enhanced, presumably due to the massive outflow in this region. On the other hand, young massive objects such as Orion-S show virtually no SO_2, in spite of a powerful outflow (Groesbeck 1994). Thus, the production of SO_2 appears to have a certain time-scale, which is not yet understood. The lack of sulfur-bearing species can be interpreted in two ways. Either the object is very young, like Orion S, or its outflow is not powerful enough to affect a large volume of the surrounding envelope and create the conditions for producing SO_2. Because of the well-developed H II region in NGC 2264, the latter explanation is more likely. The species with near-constant abundances -CS, HCO^+- appear to be good tracers of the surrounding dense cloud cores.

The high abundances of some nitrogen-bearing molecules, especially N_2, appear to be a local peculiarity. Even with a high cosmic ray ionization rate, most of the nitrogen must be in the form of N_2. Because N_2 has a long formation time scale in the gas, this would suggest that NGC 2264 is at a later stage than W 3 IRS5.

The radicals C_2H and CN are thought to be characteristics of photon-dominated regions (Fuente et al. 1995, Jansen et al. 1995). The fact that NGC 2264 has an H II region implies that it emits already copious ultraviolet photons which can photodissociate HCN and C_2H_2.

We have also compared the results for NGC 2264 with other chemical studies, in particular with other intermediate mass

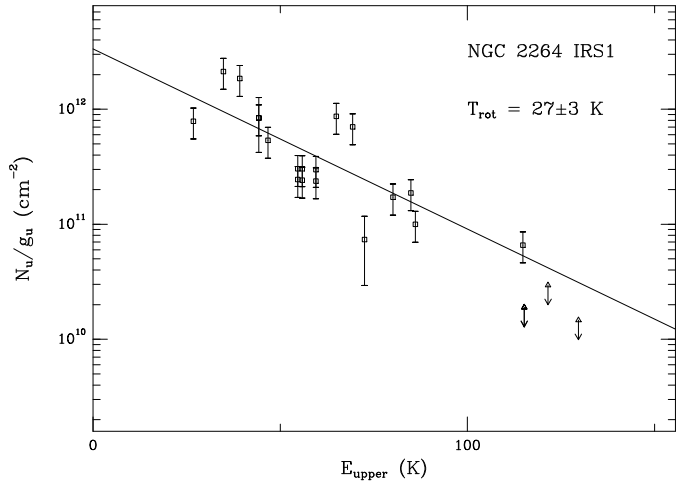

Fig. 12. Rotation diagram for methanol toward NGC 2264 IRS1. The squares are the detections, the triangles denote significant upper limits.

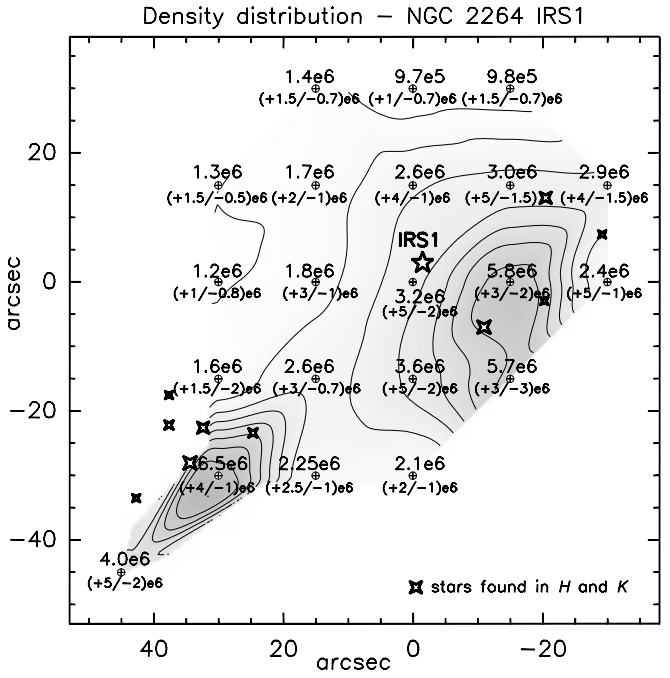

Fig. 13. The density distribution around IRS1 determined with statistical equilibrium excitation calculations point by point. The sign ⊕ indicates the positions where both CS 7→6 and CS 5→4 were obtained.

young stellar objects such as IRAS 05338-0624 and the Serpens northwestern region (McMullin et al. 1994a,b). Our study differs from theirs in two important aspects. First, McMullin et al. observed also lower-lying lines at 3 millimeter in a larger beam ($\sim 60''$), in addition to lines in the 230 GHz window. Thus, they are more sensitive to the larger scale of the cold, lower density surrounding envelope. Second, they use the dust continuum emission to constrain the total column density, rather than the optically thin CO emission. As a result, their inferred

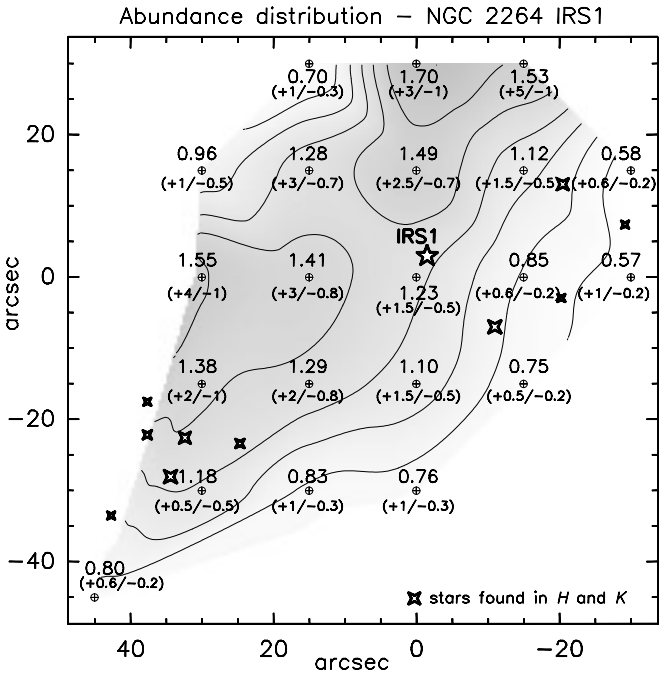

Fig. 14. The abundance distribution of CS with respect to H_2 around IRS1 averaged over a $21''$ beam. The values are given in 10^{-9}.

CO abundances are factors of 3-5 lower than our adopted values, and suggest significant depletion in the surrounding core. For NGC 2264, no evidence for depletion is found, since the CO/H_2 abundance is directly constrained to $\geq 1.7\ 10^{-4}$ by the infrared absorption line data of Lacy et al. (1994). Also, the CO column density derived from the emission line data agrees well with that seen in the pencil beam infrared absorption. Together, this again suggests that NGC 2264 is at a somewhat later stage than the objects studied by McMullin et al.

In summary, it appears that NGC 2264 IRS1 is a young stellar object which has heated its surrounding core and affected it through the outflow. Some material, especially CH_3OH, has been returned to the gas phase, but the source does not show the complex spectra characteristics of hot core regions such as Orion KL and W 3(H_2O). The lack of sulfur-bearing species and the high N_2 abundance suggest that NGC 2264 is at a later stage than W 3 IRS5, but perhaps not as late as IRS4. Further interferometric observations are required to test the distribution of the various species. The NGC 2264 results confirm the conclusion of van Dishoeck et al. (1995) based on the IRAS 16293-2422 study that the evolutionary state of the object is more important in controlling the chemistry than its luminosity.

7. Conclusions

The infrared images in J, H, and K have shown that the intermediate mass star NGC 2264 IRS1 is not the only infrared source in this region but that it is surrounded by low-mass stars. Another quite deeply embedded small star cluster is located to the southeastern side of IRS1 and can be seen in K only. IRS1

itself shows a jet-like feature to the northern direction in K. An overlay with the R-band image by Scarrott & Warren-Smith (1989) suggests a continuation of this feature, like a jet which is piercing the covering dark cloud. This scenario coincides well with the earlier assumptions that we see IRS1 "pole on".

The results of the line mapping indicate that both IRS1 and the star cluster are located inside dense molecular cloud clumps. Channel maps suggest that these clumps have slightly different central velocities of $V_{\rm LSR}$ = 6.2 km s^{-1} and of $V_{\rm LSR}$ = 8.2 km s^{-1}, respectively. Line wing maps clearly indicate two outflow systems in the observed region, one is associated with IRS1 and the second is centered at the cluster position.

The temperature and density of both cloud clumps have been estimated using statistical equilibrium excitation calculations. NGC 2264 IRS1 is located in a clump with a quite uniform gas temperature of 55 K. The CS line fits imply that there is no significant temperature decrease within an area of $1' \times 1'$. Gas which is very close to IRS1 has a temperature higher than 55 K. The clump in which the star cluster is embedded seems to have a temperature of $\geq$70 K. These two warmer regions are surrounded by more extended cloud material with a temperature between 20 to 30 K. The density is estimated to be $\sim 2\,10^6$ cm^{-3} for the gas associated with IRS1. Towards the embedded star cluster, we derive a beam-averaged density of $\geq 4\,10^6$ cm^{-3}.

CS abundance calculations provide a constant value of about $X = N({\rm CS})/N({\rm H_2}) = 1\,10^{-9}$ over the observed region. Thus, we conclude that there is no evidence on the scale of the $\sim 15''$ beam up to $1'$ for a depletion of CS. This result does not exclude a depletion of molecules on smaller scales than the single-dish beam. Interferometric observations are needed to test this.

Finally, we computed beam-averaged abundances of various molecular species at the position of IRS1. Compared with W 3 IRS5 and IRS4, the abundances of the organic molecules H_2CO and CH_3OH are somewhat enhanced, whereas those of sulfur-bearing molecules are much lower. NGC 2264 is unique compared with other objects in its nitrogen chemistry, especially the very high abundances of N_2H^+ and N_2. Taken together, these results suggest that NGC 2264 is at a somewhat later evolutionary stage.

In the future, it is important to investigate whether the physical and chemical properties found for NGC 2264 IRS1 form a special case due to its near "pole on" geometry, how they compare with other intermediate-mass stars and whether there is a clear link to the evolutionary state of these young stellar objects.

Acknowledgements. The authors are grateful to Remo Tilanus and Fred Baas for their support during the JCMT observing runs. Additionally, we thank Albrecht Sievers for all efforts of the service observation at the IRAM telescope. This work was supported by a PIONIER grant from the Netherlands Organization of Scientific Research (NWO). KS acknowledges support through the Studienstiftung des Deutschen Volkes.

References

Allen D.A., 1972, ApJ 172, L55
Allen D.A., Hyland A.R., Longmore, A.J., Caswell J.L., Goss W.M., Haynes R.F., 1977, ApJ 217,108
Assendorp R., Bontekoe, T.R., de Jonge, A.R.W., Kester, D.J.M., Roelfsema, P.R. and Wesselius, P.R., 1995, A&ASS 110, 395
Bachiller R., Liechti S., Walmsley C.M., Colomer F., 1995, A&A 295, L51
Bachiller R., in: IAU Symposium 1997: Molecules in Astrophysics, Probes and Processes, ed. E.F. van Dishoeck, Kluwer Acad. Publ., Dordrecht, p. 103
Bally J. & Lada C., 1983 ApJ 265, 824
Bessel M.S., Brett J.M., 1988, PASP 100, 1134
Blake G.A., van Dishoeck E.F., Sargent A.I., 1992, ApJ 391, L99
Blake G.A., Sandell G., van Dishoeck E.F., Groesbeck, T.D., Mundy L.G., Aspin C., 1995, ApJ 441, 689
Blake G.A., van Dishoeck E.F., Jansen D.J., Groesbeck, T.D., Mundy L.G., 1994 ApJ 428, 680
Carr J.S., Evans N.J., Lacy J.H., Zhou S.D., 1995, ApJ 450, 667
Caselli P., Hasegawa T.I., Herbst E., 1993, ApJ 408, 548
Castelaz M.W., Grasdalen G, 1988, ApJ 335, 150
Charnley S.B., Tielens A.G.G.M., Millar T.J., 1992, ApJ 399, L71
Chini R., Krügel E., Kreysa E., 1986, A&A 167, 315
de Boisanger C., Helmich F.P., van Dishoeck E.F., 1996, A&A, 310, 315
Elias J.H., Frogel J.A., Matthews K., Neugebauer G., 1982, AJ 87, 1029
Frerking M.A., Langer W.D., Wilson R.W., 1982, ApJ 262, 590
Fuente A., Martín-Pintado J., Gaume R., 1995, ApJ 442, L33
Guélin M., Langer W.D., Wilson R.W., 1982, A&A 107, 107
Greene, Young, & Walker 1990 in: Walker K.C., Adams F.C., Lada C.J., 1990, ApJ 349, 515
Groesbeck T.D., 1994, Ph.D. Thesis, California Institute of Technology
Harvey P.M., Campbell M.F., Hoffman W.F., 1977, ApJ 215, 151
Haschick A.D., Menten K.M., Baan W.A., 1990, ApJ 354, 556
Helmich, F.P., van Dishoeck, E.F., 1997, A&ASS, in press
Helmich F.P., Jansen D.J., de Graauw T., Groesbeck T.D., van Dishoeck E.F., 1994, A&A 283, 626
Henning Th., Cesaroni R., Walmsley C.M., Pfau W., 1992, A&AS 93, 525
Herbst T.M., Beckwith S.V.W., Birk C., Hippler S., McCaughrean M.J., Mannucci F., Wolf J., 1993, in Infrared Detectors and Instrumentation, ed. A.M. Fowler (SPIE Conf. 1946) (Bellingham, WA: SPIE), 605
Herbst T.M., Rayner J.T., 1994, in: Infrared Arrays: The Next Generation, eds. I.S. McLean, Kluwer Acad. Publ., Dordrecht, p. 515
Hodapp K., 1994, ApJS 94, 615
Jansen D.J., van Dishoeck E.F., Black J.H., 1994, A&A 282, 605
Jansen D.J., van Dishoeck E.F., Black J.H., Spaans M., Sosin C., 1995, A&A 302, 223
Krügel E., Chini R., 1994, A&A 287, 947
Krügel E., Güsten R., Schulz A., Thum C., 1987, A&A 185, 283
Krügel E., Densing R., Nett H., Röser H.P., Schäfer F., Schmid-Burgk J., Schwaab G., van der Wal P., Wattenbach R., 1989, A&A 211, 419
Kutner M.L., Ulich B.L., 1981, ApJ 250, 341
Lacy J.H., Knacke R., Geballe T.R., Tokunaga A.T., 1994, ApJ 428, L69
Lada C,J, 1988, in: Formation and Evolution of Low Mass Stars, eds. A.K. Dupree, M.T.V.T. Lago, Kluwer Acad. Publ., Dordrecht, p. 93
Lada C,J, Adams F.C., 1992, ApJ 393, 278
Lada C,J, Young E.T., Greene T.P., 1993, ApJ 408, 471
Mathis J.S., 1990, ARA&A 28, 37

Mauersberger R., Wilson T.L., Mezger P.G., Gaume R., Johnston K.J., 1992, A&A 256, 640
McMullin J.P., Mundy L.G., Blake G.A., 1994a, ApJ 437, 305
McMullin J.P., Mundy L.G., Wilking B.A., Hezel T., Blake G.A., 1994b, ApJ 424, 222
Mendoza E.E., Rodríguez L.F., Chavarria-K. C., Neri L., 1990, MNRAS, 246, 518
Menshchikov A., Henning Th., 1997, A&A 318, 879
Mundy L.G., Wootten HA., Wilking B.A., Blake G.A., Sargent A.I., 1992 ApJ 385, 306
Phillips J.P., Mampaso A., 1991, A&ASS 88, 189
Phillips J.P., White G.J., Rainey R., Avery L.W., Richardson K.J., Griffin M.J., Cronin N.J., Monteiro T., Hilton J., 1988, A&A 190, 289
Poynter R.L., Pickett H.M., 1984, A Submillimeter, Millimeter, and Microwave Spectral Line Catalog, NASA JPL Publ. 80-23, Revision 2.
Sandell G., Knee L.B.G., Aspin C., Robson I.E., Russell A.P.G., 1994, A&A 285, L1
Scarrott S.M. & Warren-Smith R.F., 1989, MNRAS, 237, 995
Schreyer K., Henning Th., Kömpe C., Harjunpää P., 1996, A&A 306, 267
Schwartz P.R., 1980, ApJ 238, 823
Schwartz P.R., Thronson H.A., Sten Jr., Odenwald F., Glaccum W., Loewenstein R.F., Wolf G., 1985, ApJ 292, 231
Schwartz P.R., 1987, ApJ 320, 258
Tielens A.G.G.M., Tokunaga A.T., Geballe T.R., Baas F., 1991 ApJ 381, 181
van Dishoeck E.F., Blake G.A., Draine B.T., Lunine L.I., 1993, in: Protostars and Planets III, eds. E.H. Levy, J.I. Lunine, M.S. Matthews, University of Arizona Press, Tucson, p. 163
van Dishoeck E.F., Blake G.A., Jansen D.J., Groesbeck T.D., 1995 ApJ 447, 760
van Dishoeck E.F., Blake G.A., 1995, Ap&SS 224, 237
van Dishoeck E.F., Phillips J.P., Keeme J., Blake G.A., 1992, A&A 261, L13
van Langevelde H.J., van Dishoeck E.F., Blake G.A., 1994, ApJ 425, L45
Walker C.K., Adams F.C., Lada C.J., 1990, ApJ 349, 515
Walker C.K., Maloney P.R., Serabyn E., 1994, ApJ 437, L127
Ward-Thompson D., Zylka R., Mezger P.G., 1997, in preparation
Williams J.P., de Geus E.J., Blitz L., 1994, ApJ 428, 712
Wink J.E., Duvert G., Guilloteau S., Güsten R., Walmsley C.M., Wilson T.L., 1994, A&A 281, 505
Zhou S., Evans N.J., Kömpe C., Walmsley C.M., 1993, ApJ 404, 232.

This article was processed by the author using Springer-Verlag LaTeX A&A style file *L-AA* version 3.